2013

VALIDATION OF A 'DISPLACEMENT TOMOGRAPHY' INVERSION METHOD FOR MODELING SHEET INTRUSIONS

Sarah J. Menassian
Michigan Technological University

VALIDATION OF A 'DISPLACEMENT TOMOGRAPHY' INVERSION METHOD FOR MODELING SHEET INTRUSIONS

By

Sarah Menassian

A THESIS

Submitted in partial fulfillment of the requirements for the degree of

MASTER OF SCIENCE

In Geology

MICHIGAN TECHNOLOGICAL UNIVERSITY

2013

This thesis has been approved in partial fulfillment of the requirements for the Degree of MASTER OF SCIENCE in Geology.

Department of Geological/Mining Engineering and Sciences

Thesis Advisor: *Simon Carn*

Committee Member: *Valérie Cayol*

Committee Member: *Jean-Luc Froger*

Committee Member: *Gregory Waite*

Department Chair: *John Gierke*

Table of Contents

List of Figures

Acknowledgements

Completing a dual international masters degree was an excellent experience, but certainly had its challenges. There are many people on both sides of the Atlantic that were instrumental in helping me complete the program, and in particular, this project.

Un grand merci à Valérie Cayol and Jean-Luc Froger at the Laboratoire Magmas et Volcans in Clermont-Ferrand, France for the outstanding advising and guidance, weekly Skypes, infinite emails and for hosting my visit to Saint-Etienne in 2013. It is certainly difficult to have one's primary research advisors be located thousands of miles away and I truly appreciate their willingness to take on this challenging task and dedicate time to helping me finish the project. I also greatly appreciate their sharing of codes and programs developed at the OPGC without which this project could not have been completed in two years.

I am very grateful to Ben van Wyk de Vries and Tahar Hammouda at the LMV for their help, advising and advocacy during my year in France. I also thank my fellow INVOGErs Kelly, Christine, Lucie, Estelle, Valeria, Lorenzo, Steve and Becky for their camaraderie and co-commiseration.

Many thanks to Simon Carn and Greg Waite at Michigan Tech for guidance and advising, and serving on my committee. An additional big thanks to Simon, Bill Rose and Amie Ledgerwood for help in dealing with the particularities of the INVOGE program and administrative procedures.

Big hugs to my 'Michigan family,' especially Lynn, Jason, Joanna, Mark and Travis, who made my year in the frigid north fun and calorie-filled. And who also got to experience the production of this document in living color(-ful language).

And finally, thanks to Anne and Juli for a lifetime of support, and more recently, a newfound interest in inverse deformation modeling.

Abstract

The study of volcano deformation data can provide information on magma processes and help assess the potential for future eruptions. In employing inverse deformation modeling on these data, we attempt to characterize the geometry, location and volume/pressure change of a deformation source. Techniques currently used to model sheet intrusions (e.g., dikes and sills) often require significant *a priori* assumptions about source geometry and can require testing a large number of parameters. Moreover, surface deformations are a non-linear function of the source geometry and location. This requires the use of Monte Carlo inversion techniques which leads to long computation times. Recently, 'displacement tomography' models have been used to characterize magma reservoirs by inverting source deformation data for volume changes using a grid of point sources in the subsurface. The computations involved in these models are less intensive as no assumptions are made on the source geometry and location, and the relationship between the point sources and the surface deformation is linear. In this project, seeking a less computationally intensive technique for fracture sources, we tested if this displacement tomography method for reservoirs could be used for sheet intrusions. We began by simulating the opening of three synthetic dikes of known geometry and location using an established deformation model for fracture sources. We then sought to reproduce the displacements and volume changes undergone by the fractures using the sources employed in the tomography methodology. Results of this validation indicate the volumetric point sources are not appropriate for locating fracture sources, however they may provide useful qualitative information on volume changes occurring in the surrounding rock, and therefore indirectly indicate the source location.

1. Introduction

Volcano deformation measurements form a very important component of the study and monitoring of active volcanoes. Caused as magma migrates in the subsurface and moves aside surrounding crust, deformation can help us better understand magmatic processes as well the potential for future eruptions [*Segall*, 2010]. Today, deformation is measured with radar interferometry (InSAR; [*Massonnet and Feigl*, 1998]), GPS [*Dixon et al.*, 1997], tiltmeters [*Dzurisin,* 1992], strain meters [*Dzurisin*, 2003] and leveling surveys [*Vanicek et al.*, 1980]. These data, along with models, can be used to characterize the geometry and key parameters (e.g., depth, volume, and internal pressure) of the deformation source [*Segall*, 2010].

In this project we focus particularly on surface deformation modeling. Early models seeking to identify the mechanism for observed surface deformations assumed simple geometries for the source (e.g., a sphere [*Mogi*, 1958], or an ellipsoid [*Davis*, 1986]). Assumptions were also made about the mechanical properties of the substrate, such as assuming it was an ideal elastic half-space. While these models dealt with reservoirs, *Okada* [1985] developed an analytical model for shear and tensile faults using both point and finite rectangular-shaped sources. Other models were developed allowing for more complicated geometries, such as those of *Dieterich and Decker* [1975] who used a finite element model to calculate surface deformation at volcanoes induced by magma sources of various shapes, including both reservoirs and fracture sources. Later models used mixed boundary elements allowing topography and sources of any type and shape to be taken into consideration [*Cayol and Cornet*, 1997].

All of these models, among others, form a body of 'forward models' wherein the model uses characteristics of a source to calculate the induced surface displacements. From a theoretical standpoint this is very useful as it allows us to qualitatively understand some behaviors of the studied volcano. However, to improve the monitoring of volcanoes, it is necessary to quantitatively assess the characteristics of the deformation source. Thus it is more useful to solve the inverse of these problems. That is, given a set of surface deformations, what are the characteristics of the source that could have produced them?

A range of inverse modeling techniques have been employed over the past several decades to relate observed deformation at the surface of volcanoes to volume or pressure changes occurring in the magma source in the subsurface. When sources are reservoirs, it is possible to use a method which makes no assumption on the source geometry and location. With this method, which we will refer to as 'displacement tomography,' the rock volume is discretized into regularly distributed sources. Surface displacements are linearly related to source volume changes [*Mossop and Segall*, 1999; *Vasco et al.,* 2002; *Masterlark and Lu,* 2004; *Augier,* 2012]:

$$\boldsymbol{u_{obs} = Gs} \quad \textbf{(1)}$$

where u_{obs} is a vector containing the observed surface displacements induced by n sources in the subsurface at m data points of the topography, G is an m x n Green's matrix (i.e., a matrix of surface response to unit volume/pressure change), and s is a vector containing the volume or pressure change of the n sources. This equation defines the 'forward' model for surface displacements. To solve the inverse problem, we seek the source volume changes which minimize the misfit in the least-squares sense between the data and model:

$$\boldsymbol{\chi^2 = (u_{obs} - u_{model})^T (u_{obs} - u_{model})} \quad \textbf{(2)}$$

where u_{model} is the vector of modeled surface displacements. In a geological context, particular attention must be paid to not only the model's ability to reproduce observations, but also to the feasibility of the simulated sources. From a geological standpoint, we are typically looking for a relatively smooth solution so that we do not have negative sources adjacent to positive sources, or highly positive sources next to weakly positive sources, for example. In order to enforce smoothing of volume changes, a roughness function is added to the misfit, defined as the Laplacian of volume changes:

$$\boldsymbol{R^2 = \rho^2 \|Ls\|^2} \quad \textbf{(3)}$$

where ρ^2 is a damping parameter that controls the amount of smoothing we allow in the solution, L is a Laplacian operator and s is a vector containing the volume or pressure change of the n sources. Finally, the distribution of sources which minimizes both the misfit and the roughness is determined by minimizing the sum of Equations (2) and (3) with respect to s, leading to the computation of:

$$\boldsymbol{s} = (\boldsymbol{G}^T\boldsymbol{G} + \boldsymbol{\rho}^2\boldsymbol{L}^T\boldsymbol{L})^{-1}\boldsymbol{G}^T\boldsymbol{u} \quad (4)$$

When sources are dikes, the inverse 'model' can rely on graphical relationships established in the literature to obtain a first order approximation of the position or location of a dike. For example, using figures from *Pollard et al.* [1983], we can compare the ratio of heights of the ridges formed on opposite sides of a crack caused by an intruding dike to get a first order approximation of the dip of the fracture. If displacements are symmetric about the crack, this is indicative of a vertical fracture; as the dip of the fracture changes, the displacements become asymmetric and if we determine the ratio of displacements on either side of the fracture, we can use Figure 6 [*Pollard et al.*, 1983] to estimate the dip.

For complicated surface displacements associated with open fractures, more complex methods are required. As surface displacements are non-linear functions of the source geometry and location, and a linear function of the source amplitude, some inversions are conducted in successive steps. The first step consists of inverting for the source geometry and location, defined by nine parameters [*Okada*, 1985]. This step employs a non-linear inversion method and assumes fracture displacements are constant. The second step consists of determining the volume change distribution of the source determined in the previous step by solving a linear system [e.g., *Amelung et al.*, 2000]. However there is no guarantee that the fracture determined for uniform displacement would be the same if fracture displacements were allowed to be variable. Seeking to improve the models, joint inversions are used, inverting simultaneously for geometry, location, and source amplitude distribution. One such joint inversion is a mixed boundary element model with an exploration of the parameter space using a Monte Carlo inversion method, which is a neighborhood algorithm (NA-MBEM) [*Fukushima et al.*, 2005]. With the NA-MBEM model it is necessary to make a series of *a priori* assumptions about the general location of the dike and its geometry and that the source(s) are submitted to pressures. For this model, up to 15 different parameters are required, including (among other things), the coordinates of the dike's midpoint and the dike's depth, strike, and dip. The closer to reality the initial estimate of these values, the faster the inversion will converge and the less computation power needed to reach convergence. However, the determination of 15

parameters can be numerically costly, particularly since several sources can be responsible for surface displacements. This can result in excessively long computation times, or even a failure for the model to converge.

In seeking a faster modeling technique that also required fewer *a priori* assumptions about the deformation source's geometry and location, we decided to investigate if displacement tomography [*Mossop and Segall,* 1999; *Vasco et al.,* 2002*; Masterlark and Lu,* 2004; *Augier,* 2012], thus far used for reservoirs, was also suitable for use with open fractures, such as dikes.

With this method, the relationship between the source amplitudes and the displacements are linear. Although there are more unknowns than for the inversion of fractures, solutions are obtained faster with this tomography method than with the fracture inversions. If the method works for open fractures it would allow us to simply define a grid in the subsurface, invert the source volume changes, and hone in on the location and geometry of the source. This information may satisfy our requirements, or could be used in subsequent models, such as an NA-MBEM, to refine the parameter space tested. Therefore, the motivation of this project was to test the suitability of this tomography method for modeling fracture sources.

The methodology employed in this project consisted of three steps. First, we simulated the opening of three geometrically simple dikes with different depths and dips, treating them strictly as open fractures, and calculated the resulting displacements (i.e., the forward model). For this work, we use a simple case: a flat topography and a square dike.

We next attempted to reproduce the results of these forward models using a grid of superposed point sources in the same location as the dike and undergoing the same volume changes as the dike. This step was completed because these point sources are the type of sources that will be used in the actual tomography inversions. Finally, we completed tomography inversions seeking to reproduce the volume changes induced by the dike opening.

2. Methods

This section outlines the three step methodology used in this project. For much of this work we employ MATLAB code already written by V. Cayol, J.-L. Froger, Y. Fukushima and A. Augier at the Observatoire de Physique du Globe de Clermont-Ferrand (OPGC) in Clermont-Ferrand, France. We also use the MC3 code written by *Cayol and Cornet* [1997]. Throughout this project we use a coordinate system in which the x axis corresponds to the east-west axis (east is positive), the y axis to the north-south axis (north is positive) and the z axis to the vertical direction (up is positive).

2.1. Forward model

2.1.1. Topography mesh

First we created a topographic surface on which the induced displacements should be measured. Because this validation is employing a theoretical analysis of a modeling technique, we did not use a topography representing a real area on Earth, rather we created a synthetic topography in MATLAB. We began developing the topography knowing we would be simulating a 1 kilometer long north-south striking dike located at the center of the topography.

First we calculated two concentric circles of evenly spaced points. We determined the radius of the outer circle by ensuring it was either large enough to encompass the displacements produced by the source or at least five times the width of the source [*Fukushima et al.*, 2005], whichever was larger. Ultimately, our circle had a radius of 10 kilometers. We established an inner circle with a denser point distribution to better sample the displacements where their gradients are larger (i.e., closer to the source) [*Fukushima et al.*, 2005]. The inner circle of our surface had a radius of 3 kilometers.

Once the concentric circles of points were created, a flat mesh was calculated to discretize the surface into triangular elements (Figure 2-1). The mesh is calculated with a Delaunay triangulation of the points.

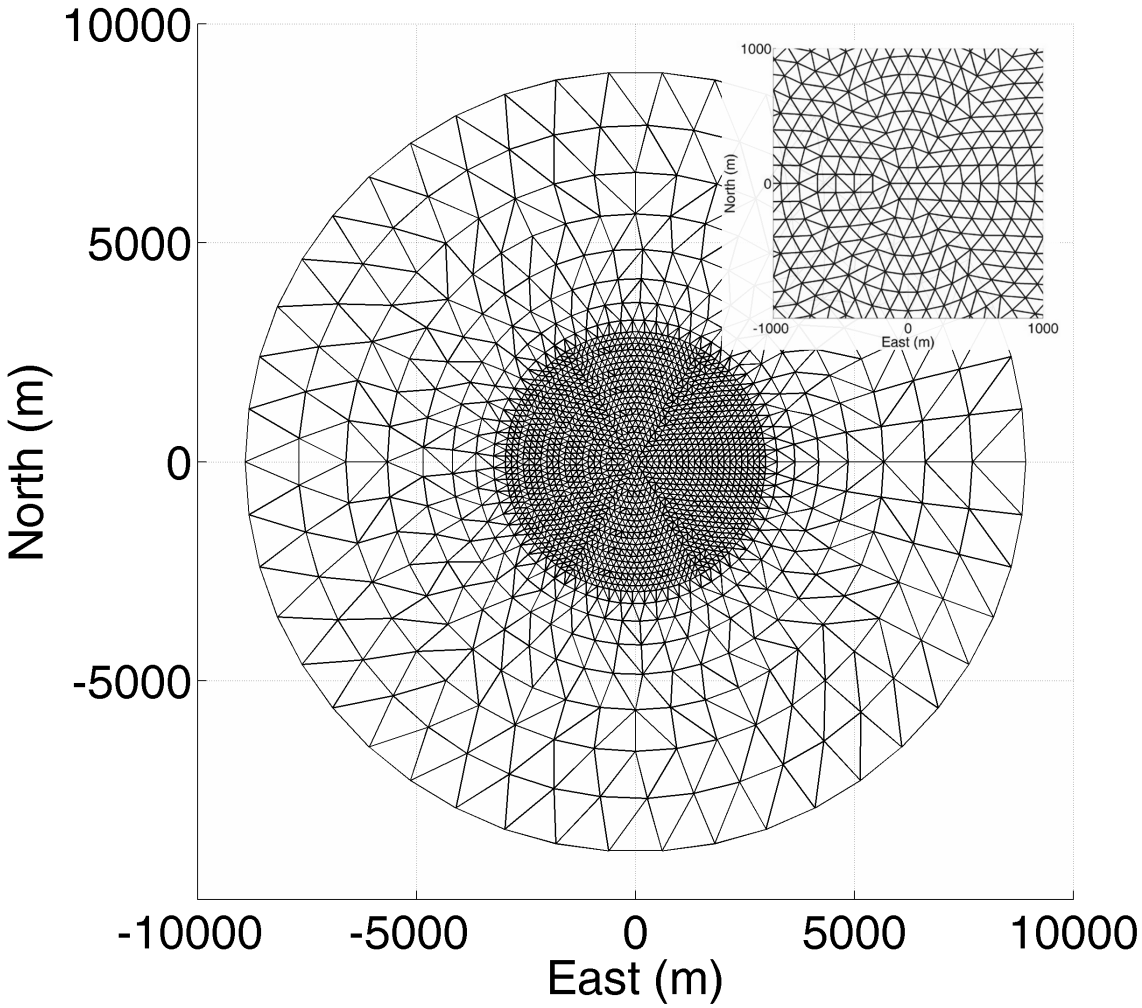

Figure 2-1. Flat topography mesh used for all subsurface dike models in this project.
Inset image zooms in on the center of the surface beneath which the synthetic dikes are situated. The surface does not represent a physical location on Earth and the coordinates are relative to the center of the surface at (0,0,0).

Because we also include a dike intersecting the surface in our set of synthetic dikes, a different surface was needed for the models involving this dike. This second surface topography mesh (Figure 2-2) was created in much the same way as described previously, however the surface mesh elements must be such that elements corresponding to the dike intersection share one side with the dike mesh elements. We placed the top side of this dike at the surface, in the center of the topography as before. It was also a north-south striking dike of 1 kilometer length. Using this geometry, the MATLAB meshing program further treated the concentric circles of points removing those that are too close to the fracture.

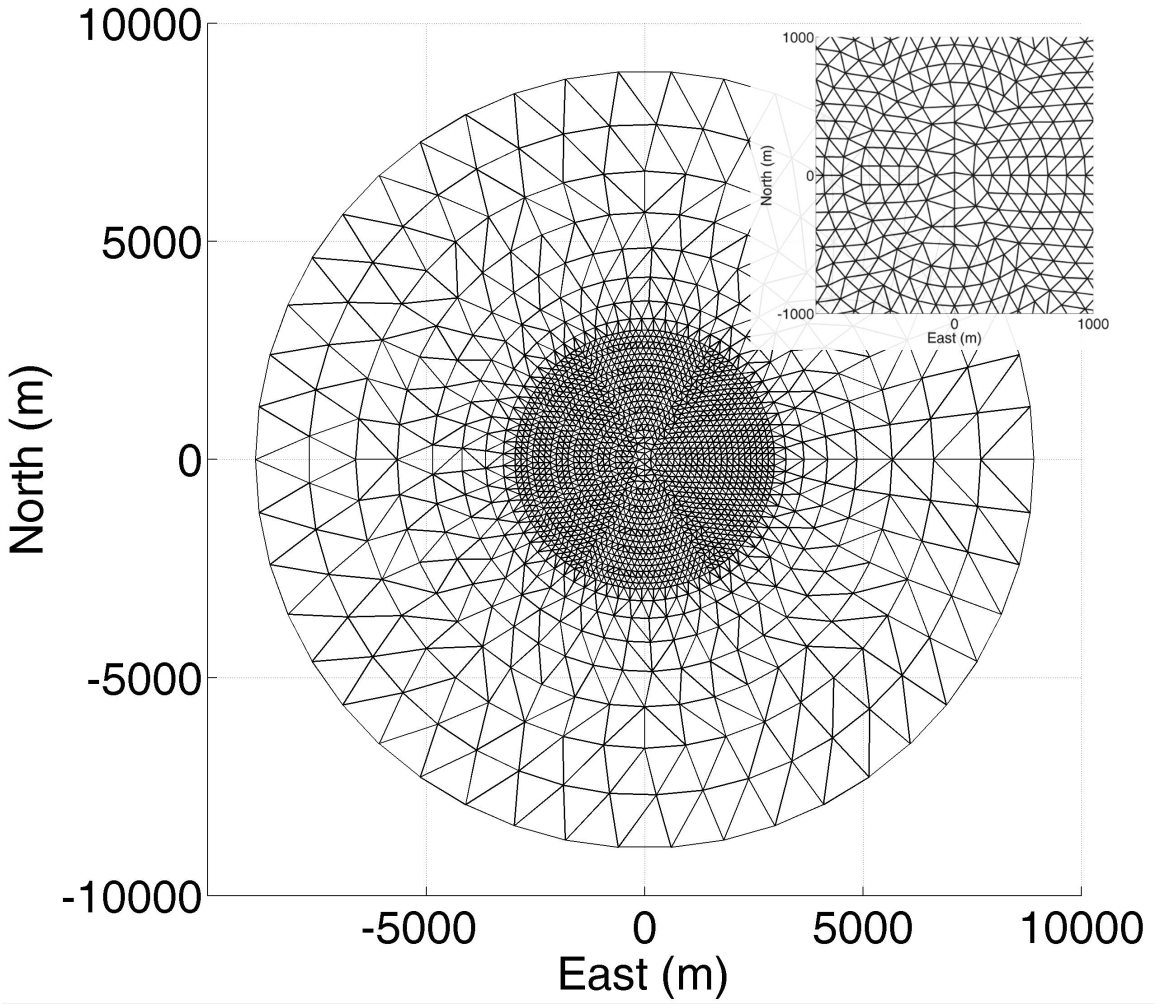

Figure 2-2. Flat topography mesh used for models involving the dike rupturing at the ground surface in this project.
Inset image zooms in on the center of the surface where the dike intersects the ground surface. The surface does not represent a physical location on Earth and the coordinates are relative to the center of the surface at (0,0,0).

2.1.2. Synthetic dikes

We next created a set of three synthetic dikes with very basic geometry. All three dikes simulated in this project were given a simple square geometry and represented as a north-south striking plane. They measured one kilometer long by one kilometer deep. Among the three models we differed the depth of the dike and its dip. Two dikes were simulated with the top of the dike at a depth of 1000 m below the surface, one with a 90 degree dip (i.e., completely vertical; Figure 2-3a-b) and the other with a 60 degree dip (Figure 2-3c-d). A third vertical dike (i.e., 90 degree dip) was simulated intersecting the ground

surface (Figure 2-3e-f). Within the square-shaped space that defined each dike, a triangular mesh was created as with the surface, as required by the program used to simulate the dike opening, MC3 [*Cayol and Cornet*, 1997].

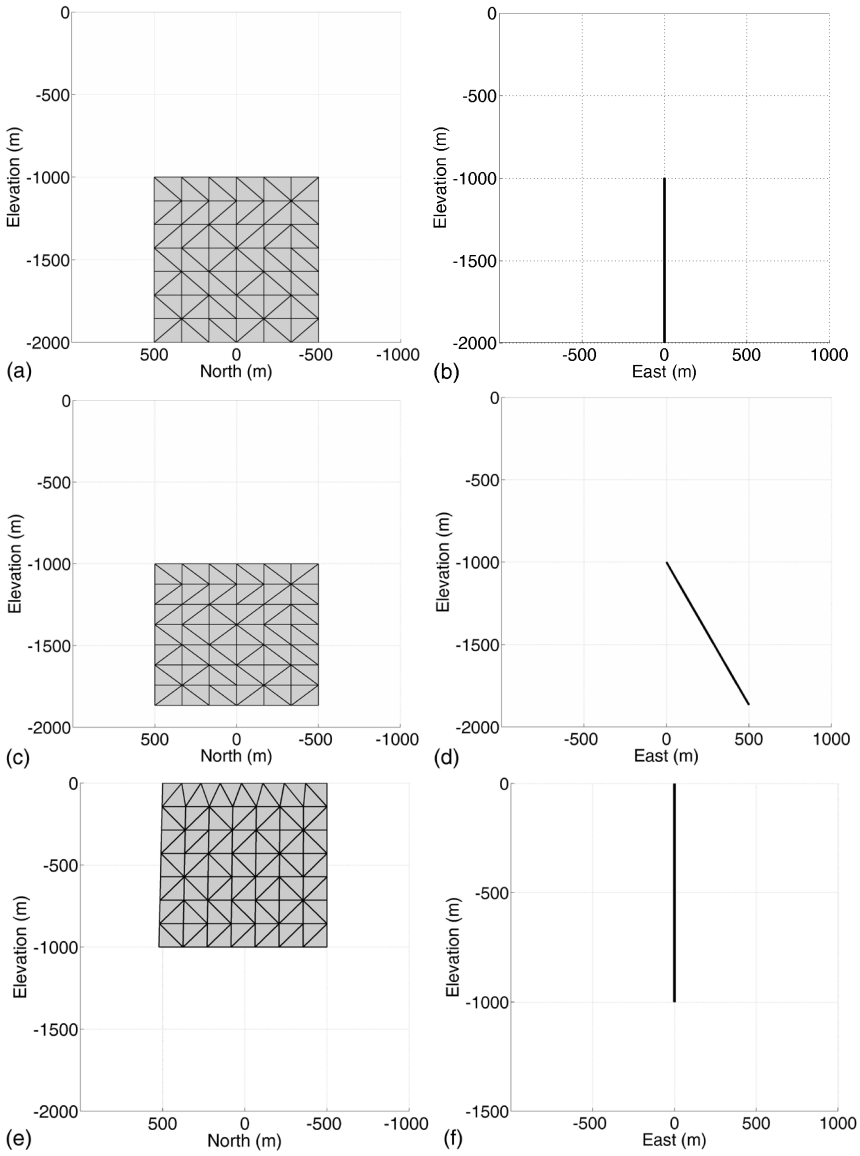

Figure 2-3. Simple synthetic dikes simulated beneath a flat surface.
Vertical dike in the subsurface–image (a) shows the east-facing view and (b) the north-facing view. Dike with 60˚ dip in the subsurface–(c) shows the east-facing view and (d) the north-facing view. Vertical dike reaching the ground surface–image (e) shows the east-facing view and (f) the north-facing view.

2.1.3. Displacement calculations

The MC3 program [*Cayol and Cornet*, 1997] is based on the combination of two boundary element methods, the Direct method [*Rizzo*, 1967], which is used for topography and reservoirs, and the Displacement Discontinuity method [*Crouch*, 1976], which is used for fractures. We used this program to calculate surface displacements induced by the opening of each of the three synthetic dikes. The resulting displacements were saved in MATLAB and subsampled to pull out discrete values to be used in comparison with tomography model results later. Using multiple components of the surface's deformation in inversions can help better resolve modeling parameters [*Wright et al.*, 2004], so we use the vertical, eastward-westward, and northward-southward components of the surface deformation.

From the MC3 results we also calculate the total opening of the fracture. Volume changes for each fracture element are computed as the displacement normal to the element, multiplied by the area of the element. The total volume change is then obtained by summing the volume changes for each element.

2.2. Reproduction of forward model with point sources

To determine if displacement tomography is appropriate for use with open fracture sources, we next attempted to reproduce the MC3 displacements with a grid of point sources in the same location as the dike, using the volume changes each element of the dike underwent in the MC3 calculations. First, we located the centroid of each element in the mesh dike. Next, we simulated a point source at each centroid calculating the induced displacement on ground surface points for each source. This calculation required a volume change for each source which we obtained from the MC3 computations (see Section 2.1.3). These volume changes are then used in the following equation [*Augier*, 2012; after *Mossop and Segall*, 1999] to calculate the displacement induced by a given source on a given ground surface point:

$$U_{cj} = \Delta V \frac{(1-\upsilon)}{\pi} \frac{(c_t - c)}{R^3} \quad \textbf{(5)}$$

$$where\ R = \sqrt{(x_t - x)^2 + (y_t - y)^2 + (z_t - z)^2}$$

where U_c is the c displacement component–c is either vertical (z coordinate), east-west (x coordinate), or north-south (y coordinate)–of the ground surface point, c_t is the ground surface point's coordinate in the c direction, c is the source's coordinate in the c direction, ν is Poisson's ratio (we assume a value of 0.25), ΔV is the volume change for the source and R is the Euclidean distance between the source and the ground surface point. The point sources are considered to be far enough apart to not interact with one another, so that their joint influence can simply be computed by summing their individual influences. Thus, displacement at each of the surface points is computed as the sum of the influence of each source.

Because the elements of the dike mesh were triangular, placing point sources at each centroid does not produce an evenly spaced grid, and such a grid is difficult to construct for the inversion. So, we also created an evenly spaced grid of points with roughly the same number of points (81) as the number of centroids (84) (Figure 2-4). We then ran the simulation on the grid with point sources at the centroids and on the regular grid.

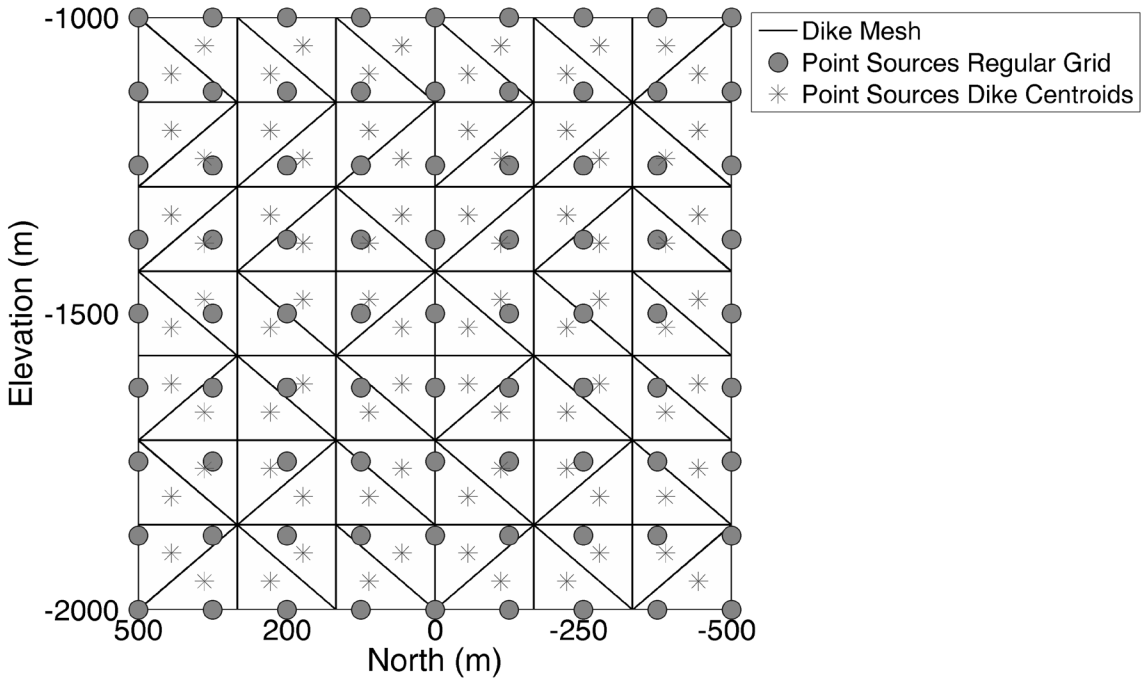

Figure 2-4. Two grids of point sources used in part two of the tomography validation for the vertical dike in the subsurface.
Dike mesh shown for reference.

Finally, we calculated the misfit in the least-squares sense between the MC3 results and the two point source runs for each dike using Equation (2) [*Fukushima et al.*, 2005].

2.3. Reproduction of volume changes via inversion

Finally, we tested the tomography method itself by inverting the surface displacements determined by MC3 in the forward models in an attempt to reproduce the volume changes corresponding to the dikes and to localize the source itself. This portion of the project makes use of a suite of MATLAB programs developed by *Augier* [2012]. We refer to these programs as the 'Tomography Toolbox' or simply, 'the toolbox.'

2.3.1. Tomography methods

Geological feasibility - model 'roughness'

In the tomography procedures we are able to control the roughness of the solution using an operator that employs the Laplacian (i.e., the second derivative of the source volume changes in space; see Equation 3). The classic form of the Laplacian operator is a 3D cross which takes into consideration the sources north, south, east and west (in the same elevation plane) of our source as well as the sources directly above and below the source of interest (see Figure 2-5a). This was the form used for most modeling runs in this project. This operator will be an *n x n* matrix, where *n* is the number of sources in the grid. The values for the columns corresponding to a source and the six adjacent sources are formed on the principles of finite difference approximations and are calculated as follows [*Masterlark and Lu*, 2004]:

Source of interest (source n*):* $-2[(\Delta x)^{-2} + (\Delta y)^{-2} + (\Delta z)^{-2}]$

***In same elevation plane as source* n:**

Sources north and south of source n*:* $(\Delta y)^{-2}$

Sources east and west of source n*:* $(\Delta x)^{-2}$

***In same N-S/E-W plane as source* n:**

Sources above and below of source n*:* $(\Delta z)^{-2}$

where Δx, Δy and Δz are the spacing between sources on the respective axes. In our software suite we always construct grids where the distance between sources is the same in all directions, so these values are always the same.

For some of the tomography models we had to use a north-south striking single plane of sources for our grid (this will be discussed in Section 2.3.2). As these grids have no sources to the east and west of the source of interest, we had to use a different Laplacian form relying on a north-south trending vertical plane. We also used this form in some models testing three plane grids (these will also be discussed in Section 2.3.2) for comparison. This Laplacian operator will differ from the cross form discussed above in that it only takes into consideration adjacent sources in the same north-south plane as the source being considered (Figure 2-5b).

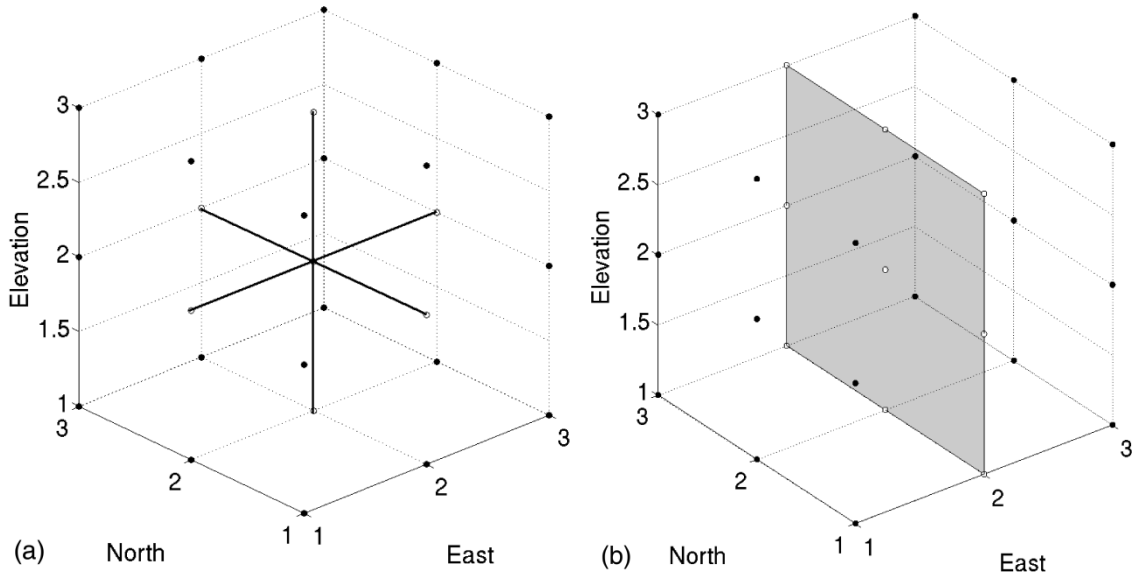

Figure 2-5. Laplacian operators used in tomography modeling.
Points included in filter are white. (a) Cross form; (b) north-south vertical plane form.

In the tomography models we varied the roughness through the use of the roughness parameter ρ^2 given in Equation (4) (and noted in $\log_{10}$ throughout this document). A lower $\log_{10}\rho^2$ value will put a premium on finding a model with a low misfit and not on smoothing the solution. Thus a lower $\log_{10}\rho^2$ will typically give us a better model, in terms of misfit, but with a geologically improbable source volume distribution.

To determine the ρ^2 value giving the best compromise between misfit and solution roughness, several methods can be used. For instance *Masterlark and Lu* [2004] use L-curves, which are curves representing the variation of the misfit (which they calculate in the root-mean-square error sense), with variations of the roughness for different values of ρ^2. The chosen ρ^2 corresponds to the minimum curvature point of the L-curve. This determination is often done visually. The toolbox [*Augier*, 2012] relies on a different method, called the Cross Validation Sum of Squares (CVSS, [*Wahba and Wang*, 1990]). This method essentially determines the predictive capability of a model corresponding to a given ρ^2 by removing one or more data points from the data set, creating a model based on the data that were not removed and then seeing how well the model can reproduce the data that were not considered in the best-fit model determination.

Non-predictability function

During an inversion, for each ρ^2, we calculate a non-predictability function using the results obtained from Equation (4). To find the 'best' model of the inversion, we seek to minimize this non-predictability function [*Augier*, 2012]:

$$NP(\beta, cvss) = \sum_{i=1}^{n} (\boldsymbol{u_i} - \mathrm{u}_{\mathbf{m}i})^{T} (\boldsymbol{u_i} - \boldsymbol{u}_{\mathbf{m}i}) \qquad \textbf{(6)}$$

where u_i are the observed displacements and u_{mi} are the modeled displacements calculated removing part of the surface points. The observed and modeled displacements are computed at surface points that were not considered in the best fit model determination using Equation (4). In this project we use two different forms of the CVSS non-predictability function. In the first, which we will refer to as the 'CVSS' method, a quarter of the points are omitted. The second form corresponds to omitting one data point at a time. For this particular CVSS, called Leave One Out (LOO), an analytical solution exists [*Matthews and Segall, 1993*]. We will refer to this as the 'LOO' method throughout this document.

For each iteration, we calculated ρ^2 with both the CVSS and LOO methods. This resulted in two 'best' models (i.e., a 'best' CVSS and LOO determination) being identified by the toolbox, so each tomography run is presented with two 'best' models.

Search Algorithm

As mentioned in the previous section, to find the best model we seek to minimize a non-predictability function. To determine with the CVSS or LOO method which ρ^2 values produce the best models, we employed a neighborhood algorithm [*Sambridge*, 1999]. We began by defining the range of possible values of ρ^2. For all models we selected a range of $\log_{10}\rho^2$ equal to -2 to 16 to test and set our convergence threshold to 0.005. That is, the model would stop when successive iterations produced models whose costs are less than 0.005% different from one another.

We set the initial number of ρ^2 values to test to 40. The toolbox program thus chooses 40 $\log_{10}\rho^2$ values from -2 to 16 to test in the initial calculations. The optimal ρ^2 value was searched for using a near neighborhood algorithm. We partition the parameter space defined by the range of these ρ^2 values into 40 values (i.e., one for each of the initial ρ^2 values to test). After the initial calculations for all 40 ρ^2 values were completed, the program looked for the ρ^2 values that produced the 10 best models (i.e., had the smallest non-predictability function value) and picked a new roughness in the neighborhood of each of these values. The model continues iterating as such, picking the best new models and resampling in the neighborhoods of the best models until the convergence threshold is met, or our maximum number of iterations (ten resampling iterations) is exceeded.

Misfit

In the tomography toolbox, the final misfit for the best models is calculated as follows:

$$\boldsymbol{Percent\ Misfit} = \frac{(\boldsymbol{u_{obs}} - \boldsymbol{u_{model}})^{\boldsymbol{T}}(\boldsymbol{u_{obs}} - \boldsymbol{u_{model}})}{(\boldsymbol{u_{obs}})^{\boldsymbol{T}}\boldsymbol{u_{obs}}} * \mathbf{100} \qquad \textbf{(7)}$$

where u_{obs} are the observed surface displacements (i.e., the MC3 results) and u_{model} are the tomography calculated surface displacements. These are the misfits we will present in the results and essentially describe what percent of the MC3 results we fail to reproduce with the models.

To quantitatively compare volume changes retrieved by the tomography inversions ($V_{inversion}$), we also calculate the percent of the MC3 dike opening volume (V_{MC3}) retrieved by the inversion:

$$\textbf{Percent Volume Retrieved} = \frac{(V_{inversion})}{(V_{MC3})} * \mathbf{100} \quad \textbf{(8)}$$

2.3.2. Localized grid tests

To be able to employ this tomography methodology, we must next create the grid of unit sources in the subsurface. We began testing grids localized where the synthetic dikes are to test the inversion's ability to reproduce quantitatively the volume changes corresponding to the MC3 computations. We started specifically with a single plane of sources (oriented north-south) located exactly where the dike was. As this was the first time a single plane grid was used by our tomography programs, it required updates to the program. The model using a single grid of sources is similar to the model from Section 3.2. The grid used for the vertical dike at depth models is presented in Figure 2-6.

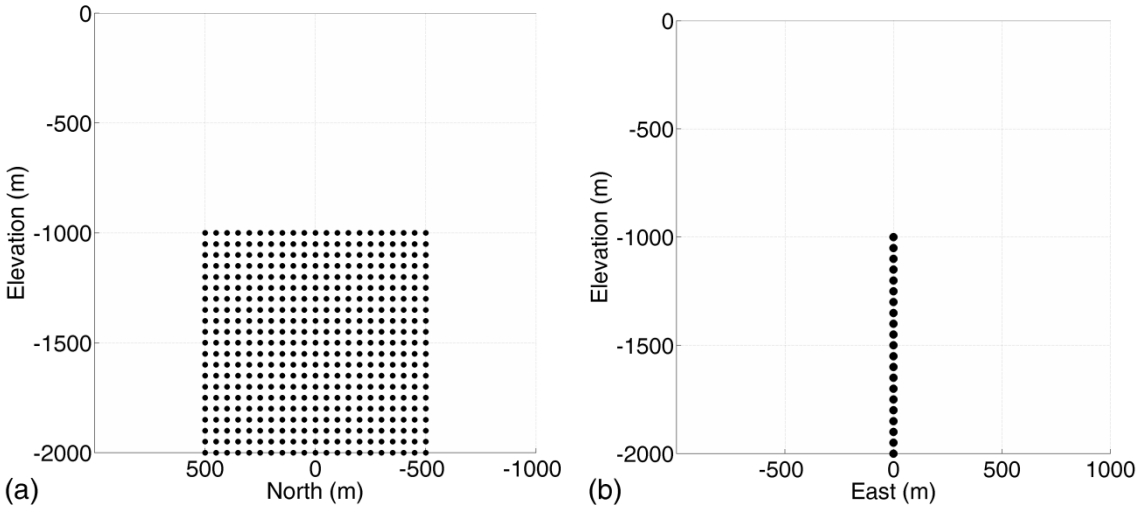

Figure 2-6. Single plane grid of unit sources used in first set of tomography inversion models for the vertical dike in the subsurface.
This grid contains 441 point sources. Image (a) shows the east-facing view and image (b) the north-facing view. The size of the points in the grid is used for illustrative purposes and not indicative of the point source radius. This value is set later when configuring the tomography model.

We also tested a grid with three north-south oriented planes, so that the grid is symmetric about the dike location. Testing a grid with three-dimensions also allowed us to compare the results produced by a two-dimensional Laplacian (as we must use for the single plane

of sources) with those produced by a three-dimensional Laplacian (see Section 2.3.1). The east-facing view of this grid is the same as for the single plane grid (Figure 2-6). The north-facing view of this grid is presented in Figure 2-7. The tomography toolbox does not allow for a slanted grid, so we conduct these localized grid tests just for the vertical dikes.

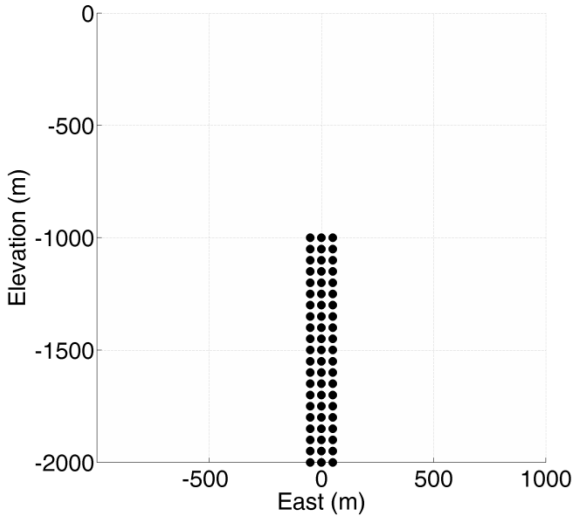

Figure 2-7. Three plane grid of unit sources used in second set of tomography inversion models for the vertical dike in the subsurface, north-facing view.
This grid contains 1323 point sources. The size of the points in the grid is used for illustrative purposes and not indicative of the point source radius. This value is set later when configuring the tomography model.

The single plane and three plane grids used for the vertical dike rupturing at the surface are the same as these grids for the vertical dike in the subsurface, with the grid extending from the dike top to the dike bottom. The single plane grid for the vertical dike reaching the ground surface contained 420 points and the three plane grid 1197 points.

We also attempted calculating models by applying a non-negativity constraint on the results of the inversion, knowing (from our MC3 results) that we are dealing with a dilating source.

2.3.3. Extended grid tests

Finally, we conducted a set of inversions with a full 3D grid that extends well beyond the extent of the dikes in all directions. For this part of the project, we aimed to see if the tomography models could not only find the dikes, but also recreate the volume changes

expected within the subsurface (which can be computed using MC3). In the z-axis (elevation) we allow the grid to approach the surface and to extend 1 kilometer below the bottom of the dike. The grid used for this set of models had 3584 points (Figure 2-8). It was used for the models for both the vertical and 60 degree dipping dikes at depth. The grid for the models involving the dike reaching the surface was located in the same coordinates along the east-west and north-south axes, however it extends 1 kilometer below the dike to only -2000 m. This grid contained 3564 points.

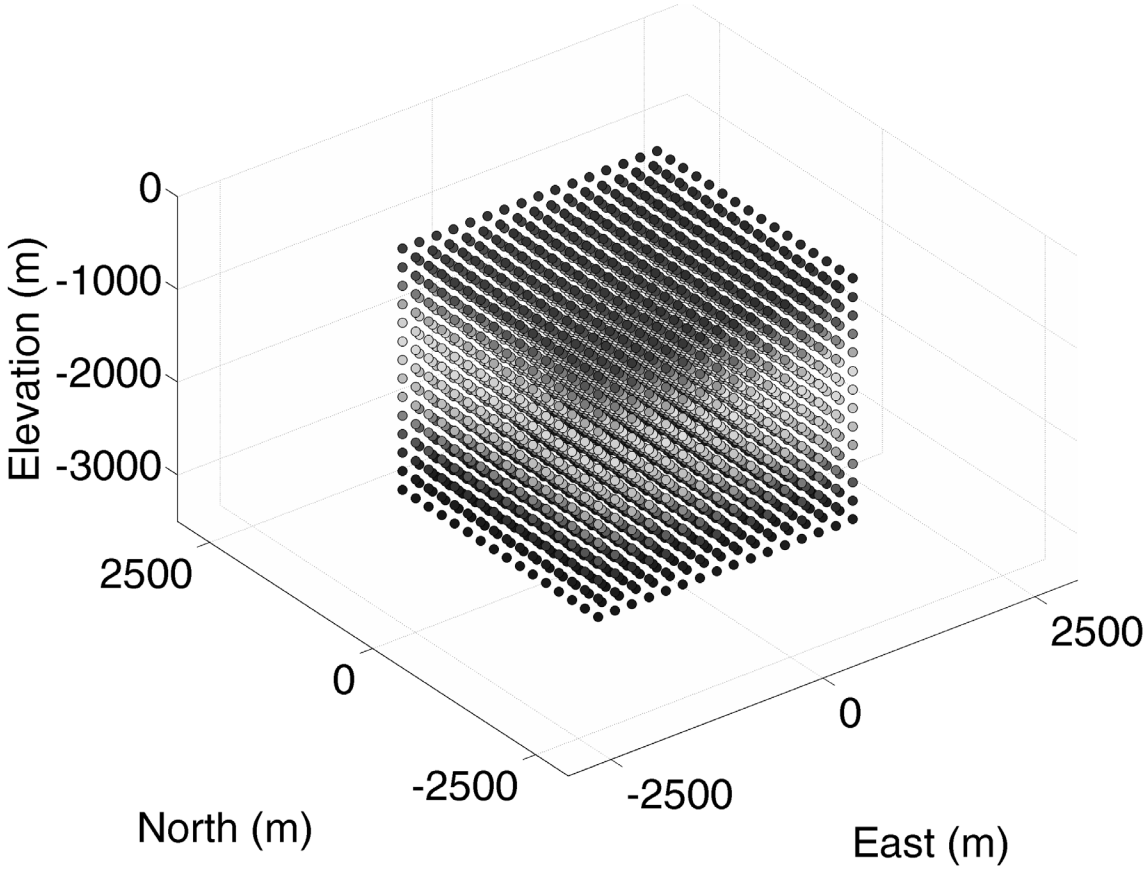

Figure 2-8. Extended grid of unit sources used in third set of tomography inversion models for dikes in the subsurface.
This grid contains 3584 point sources. The size of the points in the grid is used for illustrative purposes and not indicative of the point source radius. This value is set later when configuring the tomography model.

We did not impose a non-negativity constraint on the solution of these models as negative volume changes are expected in some parts of the surrounding rock. Indeed, *Pollard et al.* [1983] showed that as a dike dilates it shortens; this shortening is associated with volume decrease beyond the dike tips, and a volume increase along the dike walls.

Finally, as part of this exercise, we were also able to use the tomography software to focus on the most influential sources in the extended grid for the best model. This method consists of determining the number of sources needed to not decay the misfit. Using a plot produced by the software that shows the model misfit as a function of the number of sources taken into consideration in the calculation (Figure 2-9 shows an example of this plot from the extended grid test for the vertical dike in the subsurface), we visually determined the minimum number of sources needed to keep the misfit low. This allows us to minimize the model calculation time. Here we determined that 501 sources of our 3584 sources are sufficient.

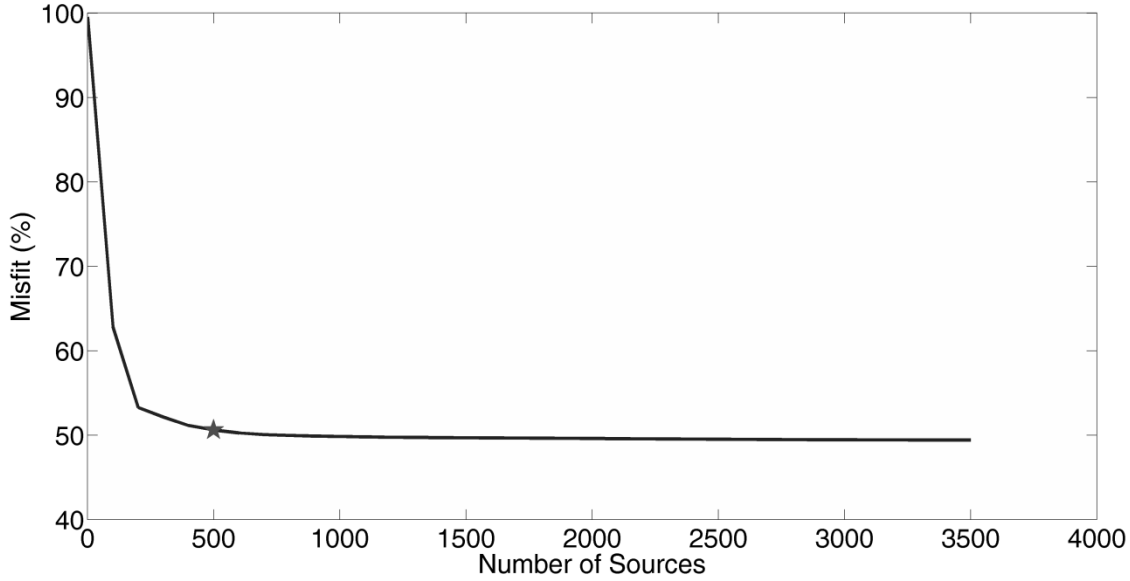

Figure 2-9. Plot of misfit versus number of sources included in the calculation for the best extended grid model for the vertical dike in the subsurface.
The star denotes where we visually identified the best compromise between number of sources (i.e., calculation time) and misfit.

3. Results

A total of eighteen models were calculated, including nine tomography inversions. In all cases, solutions converged and results were produced for each scenario tested.

3.1. Forward model

Surface displacements induced by three dikes were calculated using MC3 and displacement maps for vertical, eastward-westward, and northward-southward displacements were created for each dike. Because the displacements are calculated for synthetic dikes on a synthetic topography, we assume the data have no noise.

Total volume changes undergone by the dikes during dilation were also calculated and are presented in Table 3-1.

Table 3-1. Total volume changes undergone by dilating dikes, as computed by the MC3 program.

Dike	Volume change (m^3)
Vertical dike in the subsurface	2.0×10^5
Non-vertical dike in the subsurface	1.8×10^5
Vertical dike reaching the ground surface	2.7×10^5

In the following subsections, Figure 3-1 to Figure 3-3 will show displacements computed by MC3 for all three dikes. In these figures, we see vertical displacement patterns for the three dikes differ while eastward-westward displacement maps for all three dikes show westward displacements to the west of the dike, and eastward displacements to the east of the dike. The northward-southward displacements for all three dikes display a six lobe 'butterfly' pattern. We see surface points north of the east-west axis moving north with surface points south of the east-west axis moving south, except for along the dike. As a result of the dike shortening as it dilates, the northern part of the dike moves south, while the southern part moves north.

In this section we will also comment upon the geographical extent of the displacements. To determine the extent we divide the maximum computed displacement in a given direction by ten and any displacements below this value are not included when accounting for the extent of the displacements. Displacement extent is presented in terms of the dike's dimension (i.e., 1000 m).

3.1.1. Vertical dike in the subsurface

In terms of vertical displacements (Figure 3-1a), we see subsidence directly above the dike with uplift to the east and west. Displacements extend approximately four times the dike dimension from the dike plane in both the east and west directions. They extend almost three times the dike dimension in both the north and south directions. The eastward-westward (image b), and northward-southward (image c) displacements show the displacement patterns discussed at the beginning of Section 3.1. The eastward and westward displacements extend about 7.5 times the dike dimension to the east and west and 4.5 times the dike dimension to the north and south. Northward and southward displacements extend about six times the dike dimension to the north and south and nearly 7.5 times the dike dimension to the east and west. These displacements have the smallest amplitude as they are approximately four times less than the vertical or eastward-westward displacements.

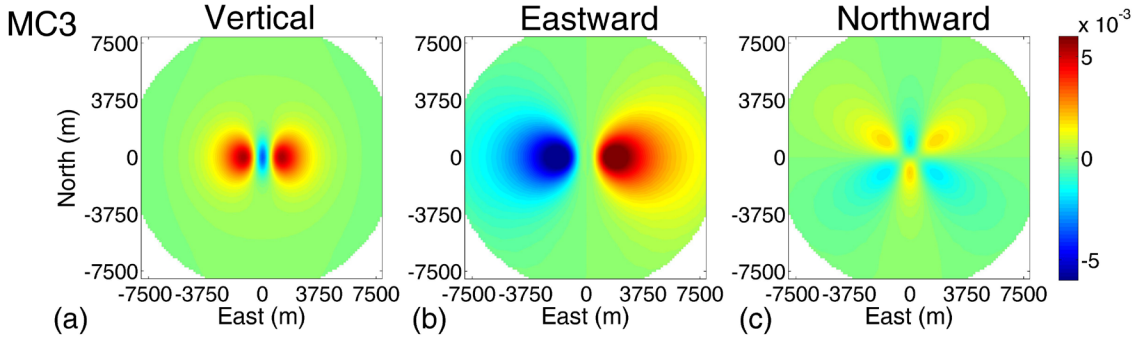

Figure 3-1. Surface displacements (m) induced by synthetic vertical dike with its upper edge at 1 km depth beneath the ground surface. Displacements are computed with MC3.

3.1.2. Non-vertical dike in the subsurface

Displacements for this dike are asymmetric about the dike plane, unlike those for the vertical dike in the subsurface. Vertical displacements induced by the opening of a 60˚ dip fracture (Figure 3-2a) show a small area of subsidence extending to about half the dike dimension west of the dike and uplift extending about 3.5 dike dimensions to the east, with the maximum uplift occurring about one dike dimension from the top of the dike. The absolute magnitude of the uplift is approximately eight times greater than the subsidence. In terms of eastward-westward displacements (Figure 3-2b), this dike produced maximum absolute eastward displacements on the same order as the maximum vertical displacements, and one order of magnitude greater than the maximum absolute westward displacements. The displacements extend about 6.5 times the dike dimension to the east, four dike dimensions to the west and three times the dike dimension to the north and south. The amplitude of the maximum northward-southward displacements (Figure 3-2c) is approximately four times less than the maximum vertical and eastward-westward displacements. The most prominent lobes are the northeast and southeast lobes. Northward-southward displacements extend about five times the dike dimension to the east, one dike dimension to the west and four times the dike dimension north and south of the dike.

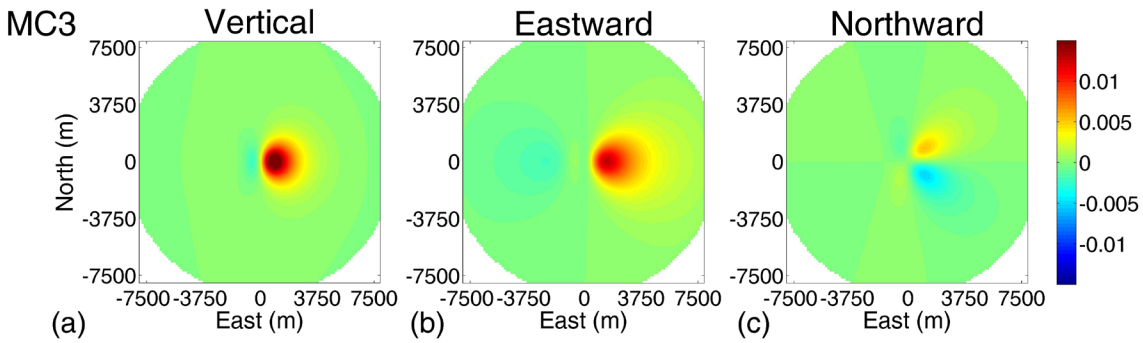

Figure 3-2. Surface displacements (m) induced by a synthetic 60˚dip dike with its upper edge at 1 km depth beneath the ground surface. Displacements are computed with MC3.

3.1.3. Vertical dike reaching the ground surface

The magnitude of the displacements in all three directions for this dike are much higher than for the dikes in the subsurface. On average, the maximum vertical displacements for this dike are 10 times higher than those for the subsurface dike, the eastward-westward displacements are about 40 times higher and the northward-southward maximum displacements are 8 times higher. The dike reaching the ground surface also produced displacements with a much more limited geographical extent than the other dikes. These displacements are also symmetric about the dike plane. The vertical displacements for this dike (Figure 3-3a) extend about one dike dimension in all directions with maximum uplift on the order of tens of millimeters. This dike produced eastward-westward displacements extending about two dike dimensions to the east and west and one dike dimension to the north and south. Maximum eastward-westward displacements are on the order of hundreds of millimeters and are approximately 2.5 times greater than maximum vertical displacements. Northward-southward displacements extend about three dike dimensions to the east and west and about two dike dimensions to the north and south. The lobes along the north-south axis are much less prominent than the other four. Similarly as for the dikes beneath the ground surface, the amplitudes of the maximum northward-southward displacements for this dike are less than the amplitudes of displacements in both other directions. The maximum northward-southward displacements are about three times less than the maximum vertical displacements, and eight times less than the maximum eastward-westward displacements.

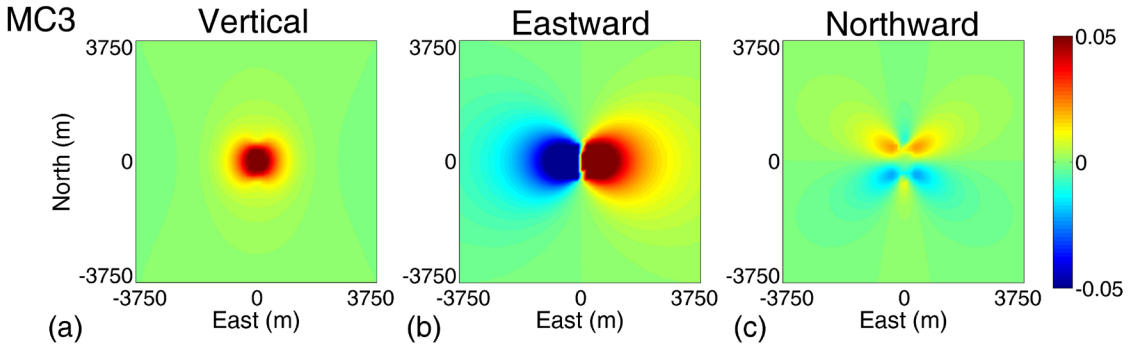

Figure 3-3. Surface displacements (m) induced by a synthetic vertical dike reaching the surface. Displacements are computed with MC3.

3.2. Reproduction of forward model displacements with point sources

Displacements induced by a grid of point sources located within the space of the three synthetic dikes were calculated. For all six grids tested we calculated overall, vertical, eastward-westward, and northward-southward misfits (Table 3-2) between surface displacements induced by the point source models and by MC3, according to Equation (7). To minimize bias in the misfit due to the inclusion of null data points (i.e., large areas where displacements are nearly zero), we limit the misfit calculations to those displacements computed by the point source grid which satisfy the criteria used in Section 3.1 to determine the geographical extent of displacements (i.e., displacements greater than the maximum absolute displacement for the direction divided by 10).

Table 3-2. Results of point source models conducted to reproduce the three forward dike models.

MODEL PARAMETERS						
MODEL	**Vertical Dike in the Subsurface**		**Non-Vertical Dike in the Subsurface**		**Vertical Dike Reaching the Ground Surface**	
Grid Type	*Centroid*	*Evenly Spaced*	*Centroid*	*Evenly Spaced*	*Centroid*	*Evenly Spaced*
MODEL MISFITS						
Overall (%)	341	270	116	120	55	49
Vertical (%)	824	649	126	139	197	112
Eastward-westward (%)	29	23	52	51	3	5
Northward-southward (%)	1500	1200	349	333	836	813

3.2.1. Vertical dike in the subsurface

The overall misfits were quite high for the grids seeking to reproduce the vertical dike in the subsurface forward model. The evenly spaced grid produced marginally better results than the centroid grid, with a lower overall misfit and better misfits for each of the three displacement directions (Table 3-2). The vertical displacements produced by the grid fail to simulate the area of subsidence directly above the dike and extend further to the north and south than the MC3 results and subsequently have a high misfit. The pattern of the eastward-westward displacements produced by the grid do match the MC3 results

relatively well, and indeed we see a much lower misfit for these displacements. However we also see the eastward-westward displacements are situated directly adjacent to the dike plane, whereas the MC3 displacements begin about half a dike dimension east and west of the dike plane. For both grids, the northward-southward displacements had significantly higher misfits than the other two directions. As seen in the displacement maps (Figure 3-4), the northward-southward displacements produced by the grid are very different from those computed by MC3. We have overall northward movement north of the dike, and southward movement south of the dike, however we are missing the important central feature that stems from the dike shortening at the tips during dilation. Further, the amplitude of the point source grid displacements is higher than the amplitude of the MC3 results.

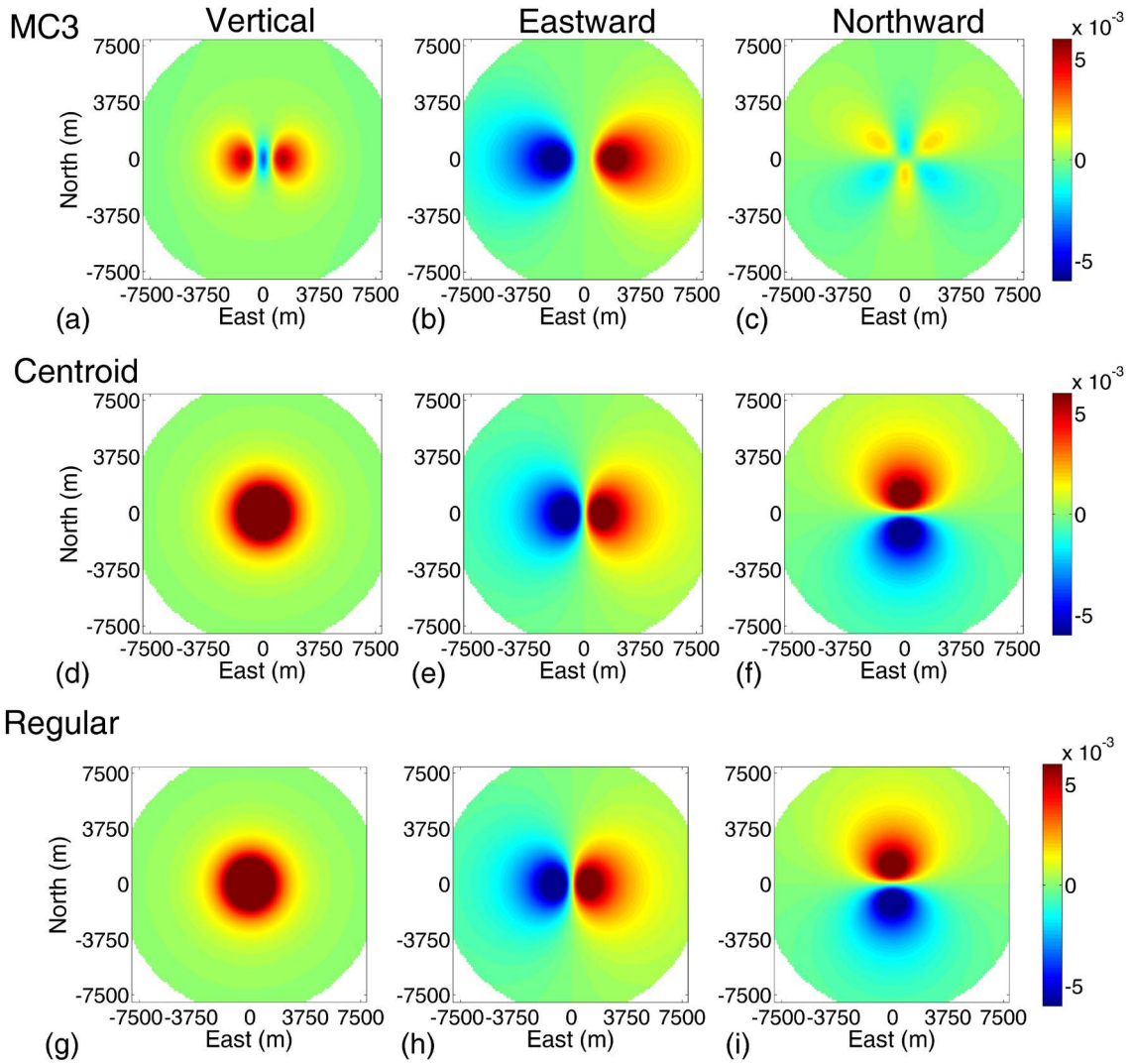

Figure 3-4. Displacements (m) produced by MC3 and grids of point sources in the space of the synthetic vertical dike in the subsurface.
Images (a)-(c) show the MC3 vertical, eastward-westward, and northward-southward displacements respectively. Images (d)-(f) show the centroid grid's vertical, eastward-westward, and northward-southward displacements respectively. Images (g)-(i) show the regularly spaced grid's vertical, eastward-westward, and northward-southward displacements respectively.

3.2.2. Non-vertical dike in the subsurface

The grids seeking to reproduce the non-vertical dike in the subsurface produced displacements with lower overall, vertical and northward-southward misfits than the grids seeking to reproduce the vertical dike in the subsurface, but higher eastward-westward misfits. Additional issues are introduced with this dike because the MC3 displacements are not symmetric about the dike plane, as is the case with the vertical dike. The point

source grids are not able to reproduce this asymmetry for any of the displacement directions. For all three directions we also see similar problems with the patterns of displacements produced by these grids (Figure 3-5) as we did with the previous grids (Figure 3-4).

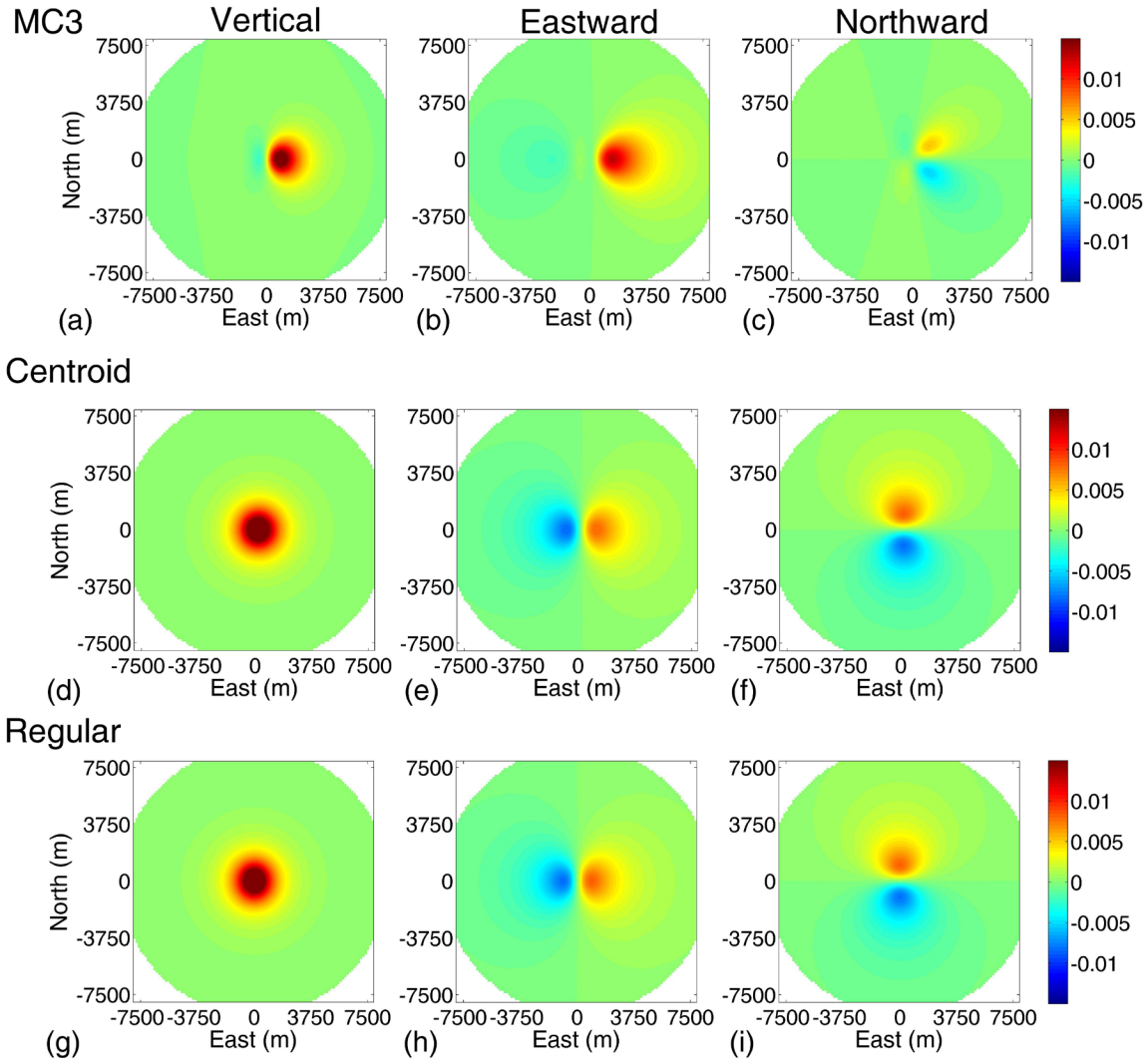

Figure 3-5. Displacements (m) produced by MC3 and grids of point sources in the space of the synthetic non-vertical dike in the subsurface.
Images (a)-(c) show the MC3 vertical, eastward-westward, and northward-southward displacements respectively. Images (d)-(f) show the centroid grid's vertical, eastward-westward, and northward-southward displacements respectively. Images (g)-(i) show the regularly spaced grid's vertical, eastward-westward, and northward-southward displacements respectively.

3.2.3. Vertical dike reaching the ground surface

Finally, for the point source grids attempting to reproduce the vertical dike reaching the ground surface, we see the lowest of our overall misfits. Because this dike reaches the surface, we do not see the same area of subsidence directly above the dike as with the vertical dike in the subsurface. Therefore, these point source grids were better able to reproduce the vertical displacements, though did not reproduce the exact shape of the MC3 results. These grids also produced eastward-westward displacements with very low misfits (nearly zero); indeed the eastward-westward displacements (Figure 3-6,e,h) match the MC3 results well. This regularly spaced grid produced the lowest misfit for the northward-southward displacements out of all the other models however, as with the other grids, we fail to reproduce northward-southward displacements. Further, the magnitude of the northward-southward displacements are much higher than the MC3 results.

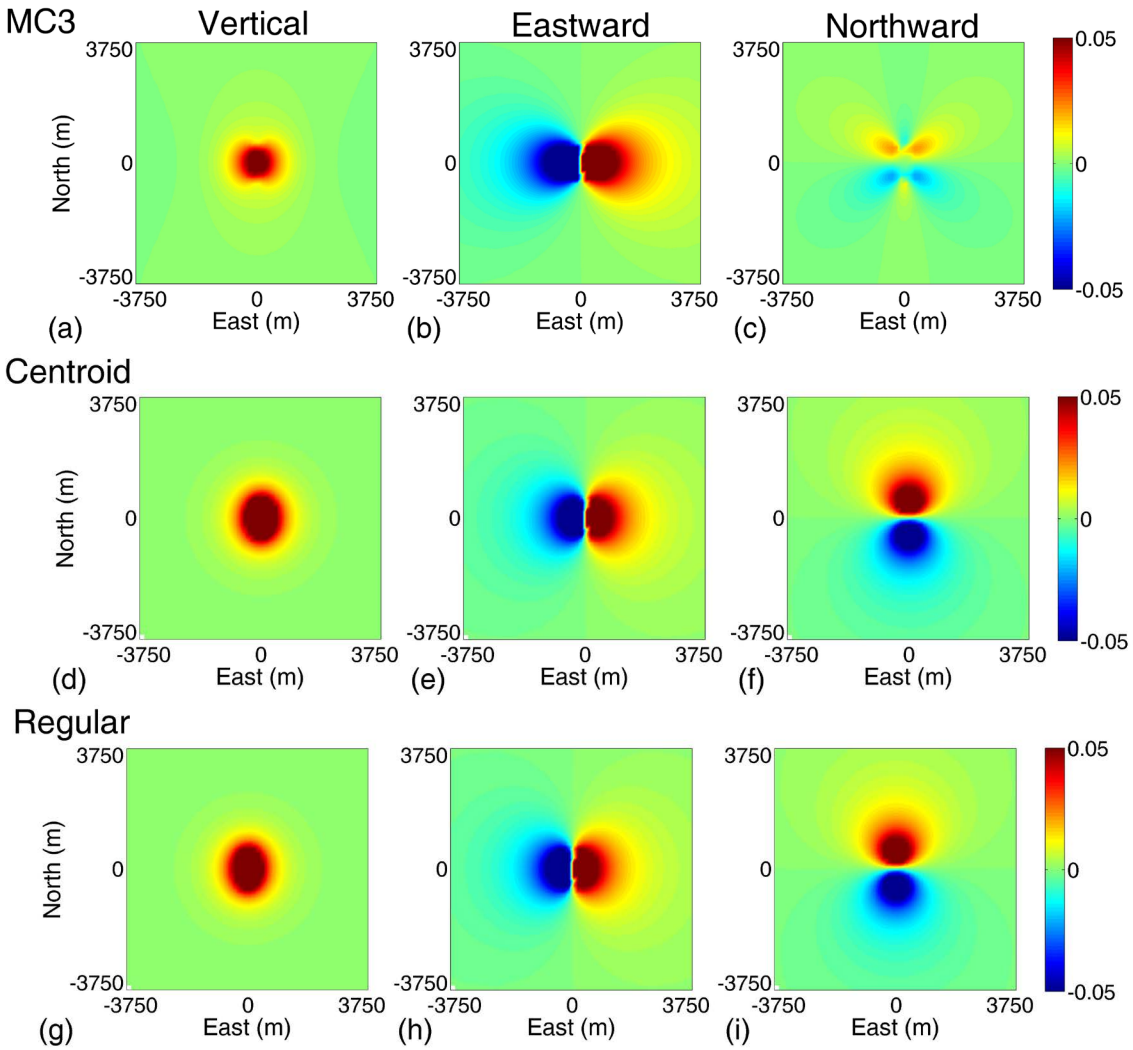

Figure 3-6. Displacements (m) produced by MC3 and grids of point sources in the space of the synthetic vertical dike reaching the surface.
Images (a)-(c) show the MC3 vertical, eastward-westward, and northward-southward displacements respectively. Images (d)-(f) show the centroid grid's vertical, eastward-westward, and northward-southward displacements respectively. Images (g)-(i) show the regularly spaced grid's vertical, eastward-westward, and northward-southward displacements respectively.

3.3. Reproduction of volume changes via inversion

Nine inversions were calculated in which we attempted to retrieve the dike volume changes with point sources. As noted in Section 2.3.1, the tomography toolbox determines the 'best' model of an inversion using a non-predictability function. We used both methods (i.e., CVSS and LOO) to retrieve the best ρ^2 and thus will present two 'best' models for each inversion.

3.3.1. Vertical dike in the subsurface

Overall the tomography inversions for the vertical dike in the subsurface found models with decent misfits, but all underestimated the volume change undergone by the dike opening by at least 50% (Table 3-3). The $\log_{10}\rho^2$ values varied among the iterations, with the single plane grid producing the roughest solutions and the extended grid producing the smoothest solution.

We attempted to impose a non-negativity constraint on the solutions for the best models however this failed to converge. Tolerances were well above the default value used in MATLAB (on the order of 10^{-7}; this value depends on the inputs). Using a tolerance of 100 the solution did converge, but produced volume changes of 0 throughout the entire grid, indicating that the null model gives the best fit.

In subsequent sections we will present the displacement maps and the source volume change distribution for the best models for each grid type. For the extended grid, we will also discuss how the source volume distribution changes when we consider only the most influential sources.

Table 3-3. Results of tomography inversion models conducted to reproduce the vertical dike in the subsurface.

MODEL PARAMETERS								
MODEL	**1**	**1**	**2**	**2**	**3**	**3**	**4**	**4**
Grid Shape	1- plane	1- plane	3- plane	3- plane	3- plane	3- plane	Extended	Extended
Cost Function	CVSS	LOO	CVSS	LOO	CVSS	LOO	CVSS	LOO
Laplacian	N-S Plane	N-S Plane	Cross	Cross	N-S Plane	N-S Plane	Cross	Cross
ρ^2 (log_{10})	2.6	2.4	7.2	4.9	7.8	7.9	9.5	7.5
Volume Change (m^3)	$-3x10^5$	$-3x10^5$	$5x10^4$	$6 x10^4$	$5x10^3$	$1x10^5$	$1x10^5$	$1x10^5$
MODEL MISFITS								
Overall (%)	46	45	51	48	52	53	65	49
Vertical (%)	42	43	36	36	46	50	66	34
Eastward-westward (%)	39	39	47	44	46	46	60	46
Northward-southward (%)	127	126	136	134	138	139	116	136
Volume changes retrieved (%)	-150	-150	25	30	2	50	50	50

3.3.1.1. Localized grid test - single plane grid

For the single plane grid test for a vertical dike at depth, the best models determined by both methods had very similar $\log_{10}\rho^2$ values, and subsequently similar results. The total misfits for both were relatively reasonable at values around 45% (Table 3-3), however both produced negative overall volume changes, which does not correspond with the MC3 results.

The vertical displacements produced by this inversion are able to simulate uplift to the east and west of the grid, with subsidence directly above (Figure 3-7d,g). The largest feature in the eastward-westward displacements is the area of westward movement to the west of the dike, and eastward movement to the east (Figure 3-7e,h). This aligns with the

MC3 results (Figure 3-7b), however the small areas of opposite movement adjacent to the dike are not expected. Finally, the northward-southward displacements (Figure 3-7f,i) do not match the MC3 results (Figure 3-7c) well at all, and this is reflected in the elevated northward-southward misfits for both best models. As with the point source grid model results, most noticeably absent are the areas of movement directly north and south of the dike where we expect to see movement towards the center of the dike as the dike shortens during dilation.

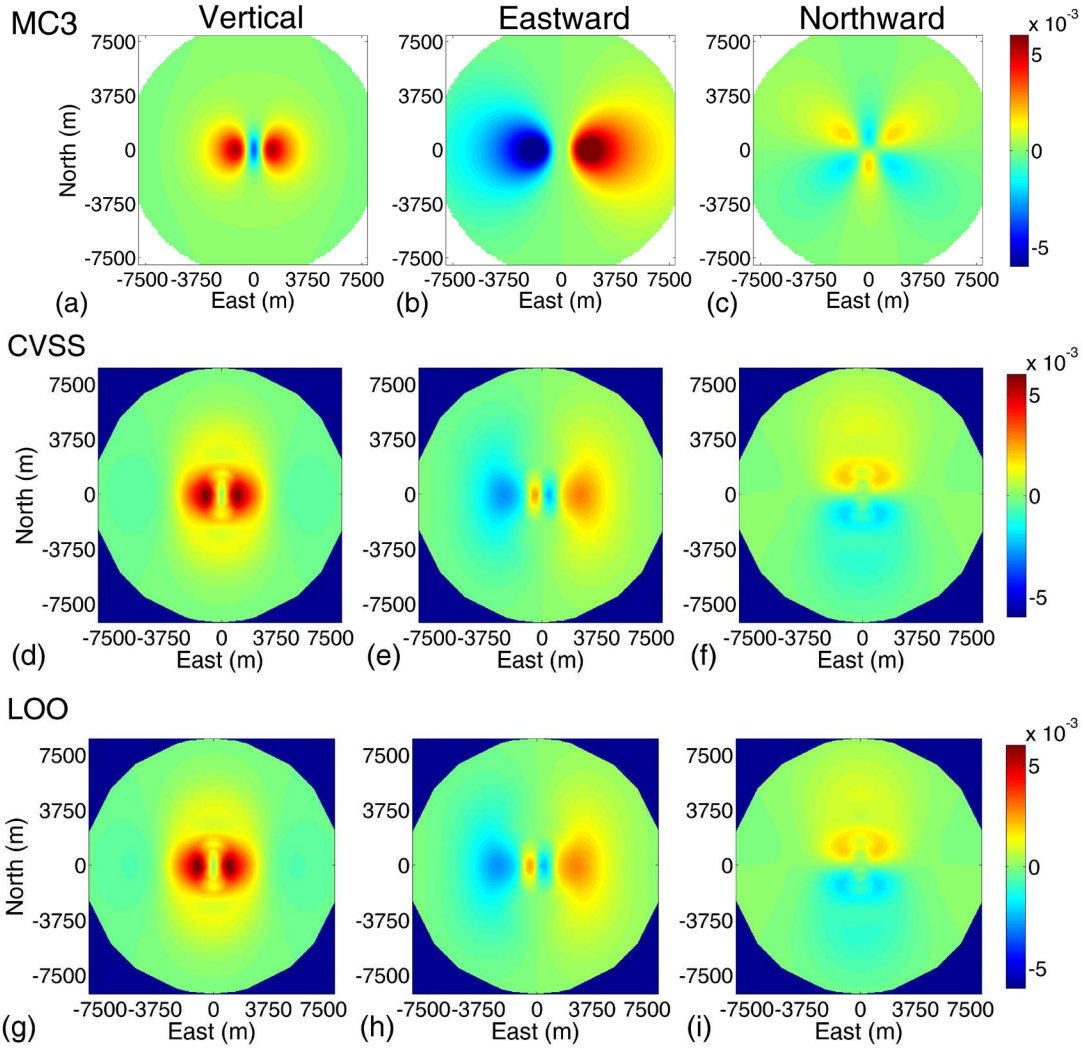

Figure 3-7. Displacements (m) produced by the best models for the single plane grid inversion run to reproduce the vertical dike in the subsurface.
Images (a)-(c) show the MC3 vertical, eastward-westward, and northward-southward displacements respectively. Images (d)-(f) show the CVSS method best model's vertical, eastward-westward, and northward-southward displacements respectively. Images (g)-(i) show the LOO method best model's vertical, eastward-westward, and northward-southward displacements respectively.

Both of the source volume distributions for the two best models are relatively rough and include both positive and negative volume changes (Figure 3-8). Further, both the CVSS and LOO methods produced very large volume changes for the individual point sources (on the order of 10^8 m^3). These individual source volume changes are greater than the total dike opening computed by MC3. Therefore, while the misfits for these two models were relatively reasonable, the sources found are geologically improbable.

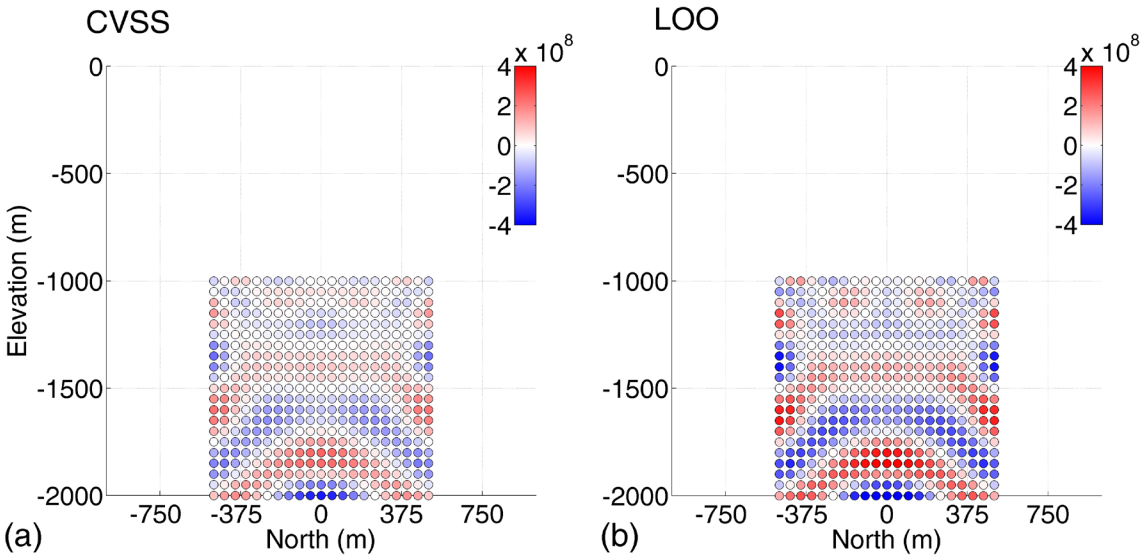

Figure 3-8. Source volume distributions (m^3) for the best single plane grid models for the vertical dike in the subsurface.
Image (a) shows the CVSS results and image (b) the LOO results.

For this grid, and the other localized grids, when we attempted to focus on the most influential sources we found the plot of misfit versus the number of sources included in the calculation was nearly linear, so all sources needed to be included to get the smallest possible misfit.

3.3.1.2. Localized grid test - three plane grid

For this test, we conducted two models using the two different Laplacian operators (see Figure 2-7). Using the 'cross' operator (i.e., the 3D operator; Figure 2-5a), both the CVSS and LOO methods lead to results with higher $\log_{10}\rho^2$ values (Table 3-3) than the single plane grid model (i.e., smoother solutions). The two $\log_{10}\rho^2$ values differed by about 3 units with the CVSS solution smoother than the LOO solution. Nevertheless, both

methods found models with misfits of around 50%, with the LOO misfit slightly lower than the CVSS misfit.

The vertical displacements produced by this inversion (Figure 3-9d,g) are relatively good but fail to reproduce the area of subsidence directly above the dike. These models produced eastward-westward displacement patterns (Figure 3-9e,h) similar to those of the single plane grid, with large areas of westward movement to the west of the dike, and eastward movement to the east as well as unexpected small areas of opposite movement adjacent to the dike. As with the single plane inversion, we also see northward-southward displacements (Figure 3-9f,i) that do not match the MC3 (Figure 3-9c) results well. Again, most noticeably absent are the areas of movement directly north and south of the dike, where we expect to see movement towards the center of the dike as the dike shortens during dilation.

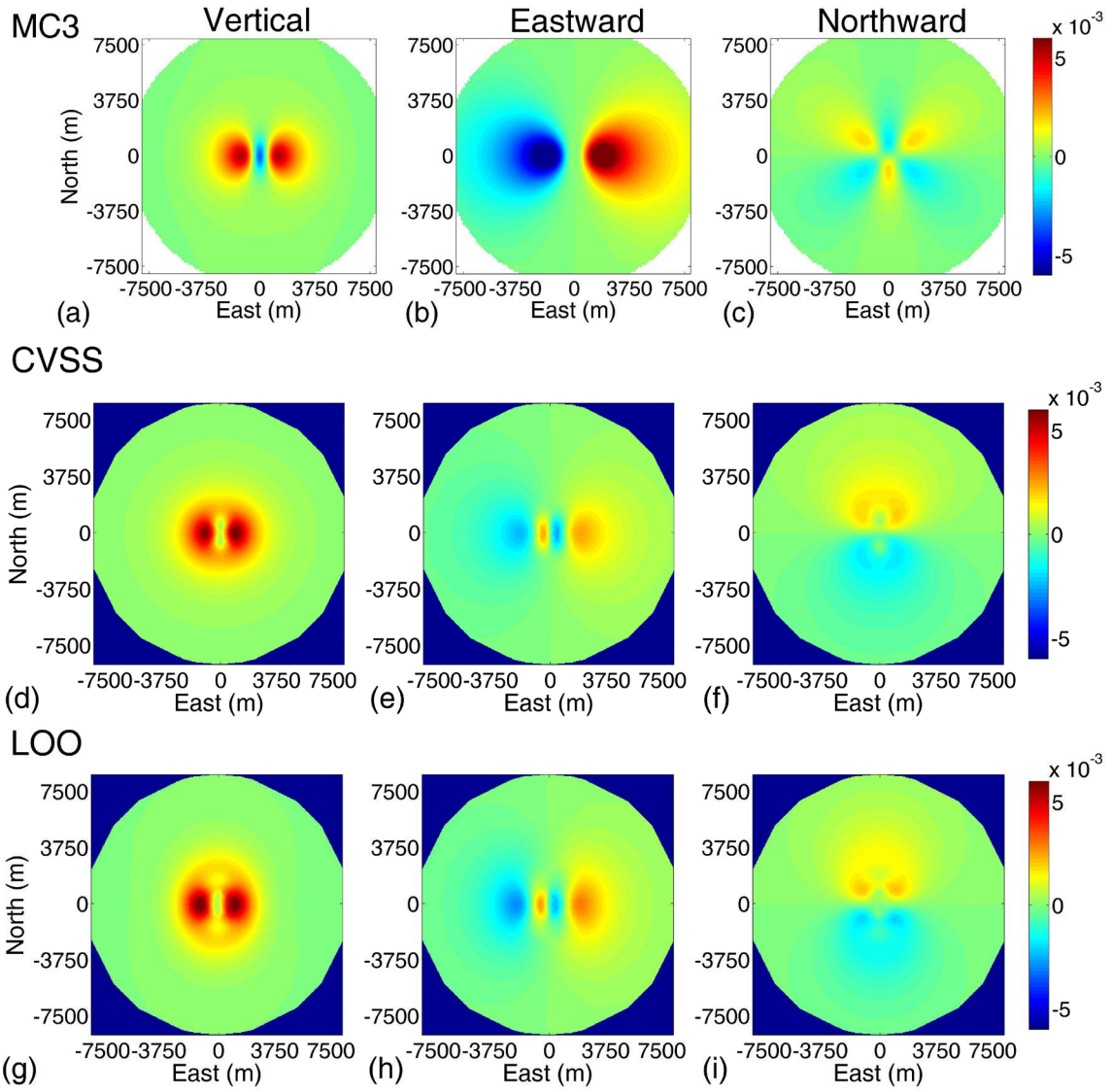

Figure 3-9. Displacements (m) produced by the best models, using the cross-shaped Laplacian, for three plane grid inversion run to reproduce the vertical dike in the subsurface.
Images (a)-(c) show the MC3 vertical, eastward-westward, and northward-southward displacements respectively. Images (d)-(f) show the CVSS method best model's vertical, eastward-westward, and northward-southward displacements respectively. Images (g)-(i) show the LOO method best model's vertical, eastward-westward, and northward-southward displacements respectively.

The CVSS method, having a higher $\log_{10}\rho^2$ value, found a smoother solution (Figure 3-10a) than the LOO method, with volume changes several orders of magnitude lower than the LOO solution, which itself is quite rough. Both solutions include negative volume changes, which we do not see in the MC3 results. Further, the LOO solution includes individual source volume changes on the same order of magnitude as the total

dike opening computed by MC3. As with the single plane inversion, while the misfits for these two models are reasonable, the sources found are not probable.

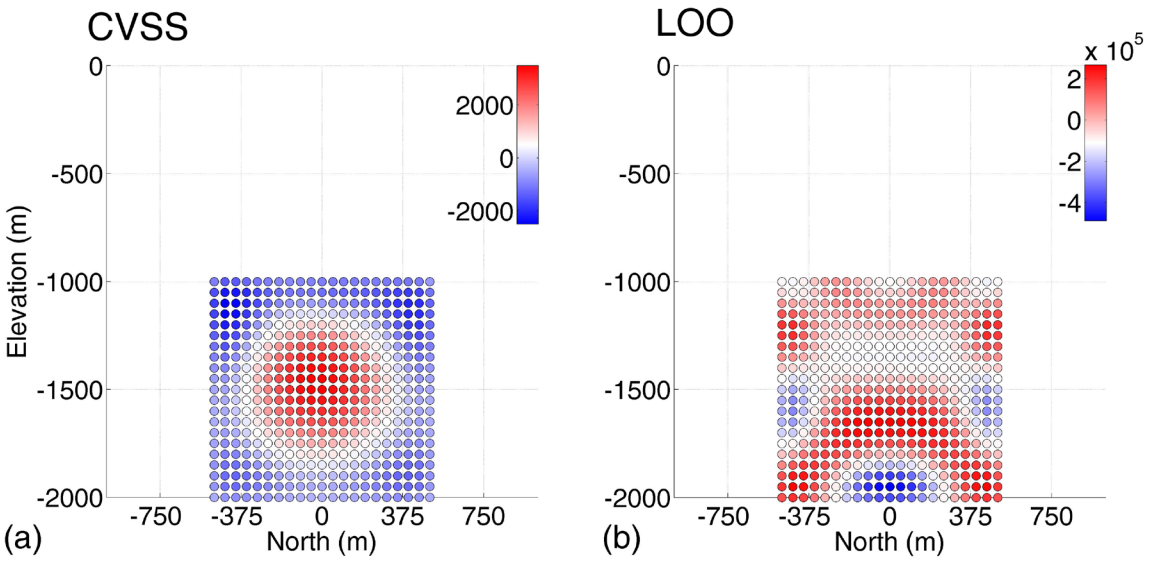

Figure 3-10. Source volume distributions (m^3) on the dike plane for the best three plane grid models, using the cross-shaped Laplacian, for the vertical dike in the subsurface.
Image (a) shows the CVSS results and image (b) the LOO results.

Using the north-south plane Laplacian operator (i.e., the 2D operator; Figure 2-5b), the best models determined by the two cost functions had nearly the same $\log_{10}\rho^2$ value. This value is also close to that for the best model found by the CVSS method with the 3D Laplacian. The two best models found with the 2D Laplacian also had reasonable overall misfits around 52%. The style of displacements produced by both best 2D Laplacian models (Figure 3-11) are very similar to those produced with the 3D Laplacian operator for the same grid (Figure 3-9). As with all results seen thus far, vertical and eastward-westward displacements produced by the inversions share many similar features with the MC3 results, but the northward-southward displacements have some fundamental issues.

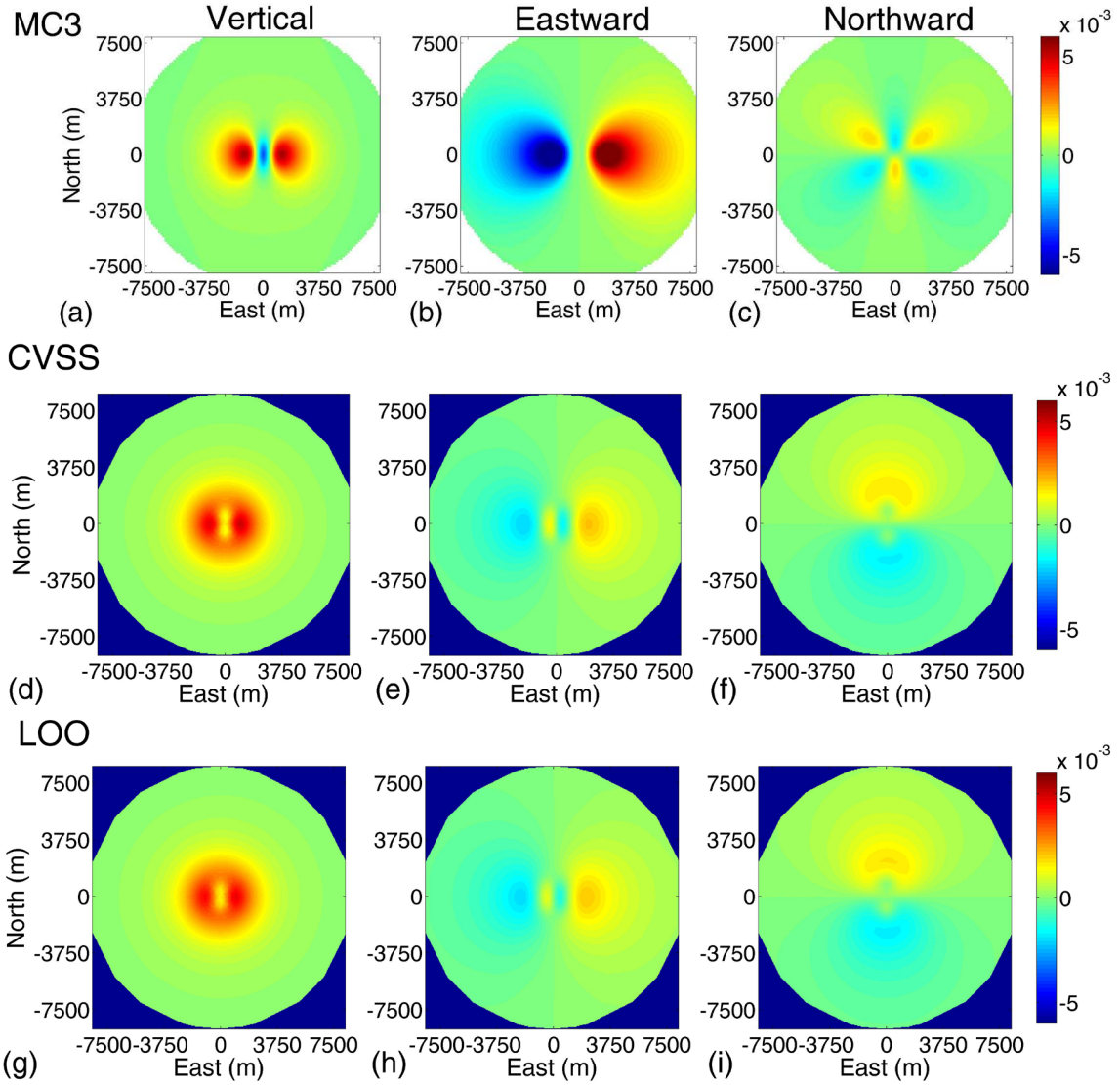

Figure 3-11. Displacements (m) produced by the best model using the north-south plane shaped Laplacian, for the three plane grid inversion run to reproduce the vertical dike in the subsurface. Images (a)-(c) show the MC3 vertical, eastward-westward, and northward-southward displacements respectively. Images (d)-(f) show the CVSS method best model's vertical, eastward-westward, and northward-southward displacements respectively. Images (g)-(i) show the LOO method best model's vertical, eastward-westward, and northward-southward displacements respectively.

Both models had similar $\log_{10}\rho^2$ values and thus have similar source volume distributions (Figure 3-12). As with previous results, both solutions include negative volume changes, which we do not see in the MC3 results, however both models did simulate volume changes of a more reasonable order of magnitude than some of the previous inversions (e.g., 10^3 m^3 as opposed to 10^{10} m^3). With these models we do see negative volume changes at the upper ends of the grid (i.e., where the dike tips would be). As discussed

previously, we expect the dike to shorten at the tips as the dike dilates, however as seen in Figure 3-11 (images f and i), we do not see the northward-southward displacement patterns this should induce.

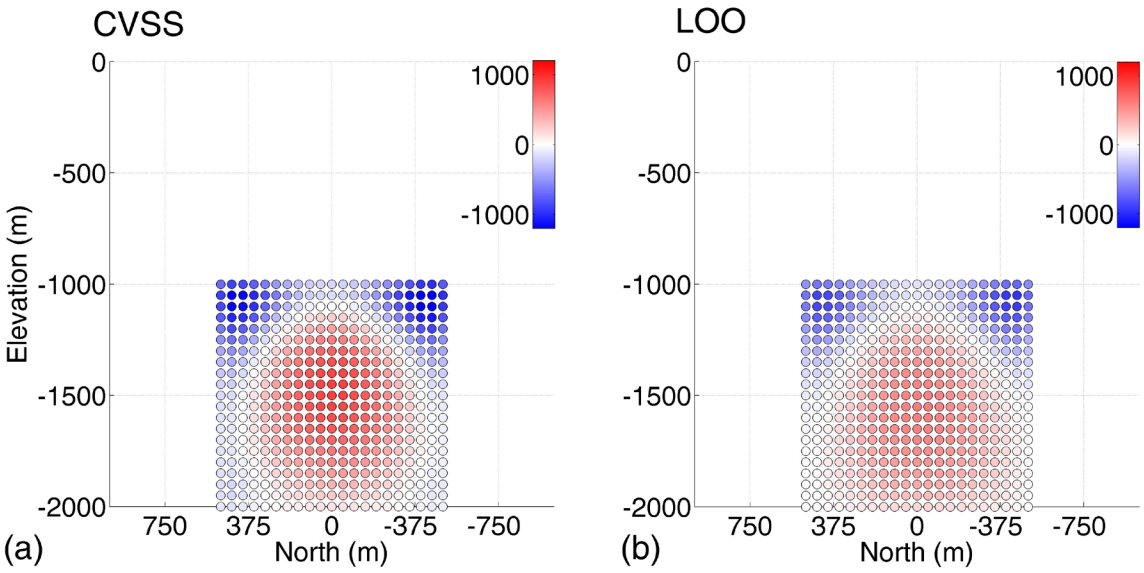

Figure 3-12. Source volume distributions (m^3) on the dike plane for the best three plane grid models, using the north-south plane shaped Laplacian, for the vertical dike in the subsurface.
Image (a) shows the CVSS results and image (b) the LOO results.

3.3.1.3. Extended grid test

For the extended grid test of a vertical dike at depth, the best models determined by both the CVSS and LOO methods had relatively smooth solutions with $\log_{10}\rho^2$ values higher than 7. The best CVSS model for this grid had the highest $\log_{10}\rho^2$ value among all inversions seeking to find the vertical dike in the subsurface; this $\log_{10}\rho^2$ value is about 2 units higher than the LOO result for this inversion. The misfits for these two models also differed by about 15%, with the LOO method finding the solution with a lower overall misfit. The LOO solution also had lower misfits in the vertical and eastward-westward directions, however its northward-southward misfit was higher than the CVSS solution.

The vertical displacements produced by the CVSS solution (Figure 3-13d) do not match the MC3 results (Figure 3-13a) well, though the LOO model vertical displacements (Figure 3-13g) are better. Both models produced eastward-westward displacements (Figure 3-13e,h) with large areas of westward movement to the west of the dike, and eastward movement to the east, however the LOO model also simulated the unexpected

small areas of opposite movement adjacent to the dike, as did all of the localized grid best models. As with all localized inversions for this dike, we also see northward-southward displacements (Figure 3-13f,i) that do not match the MC3 results well, most noticeably missing the areas of movement directly north and south of the dike.

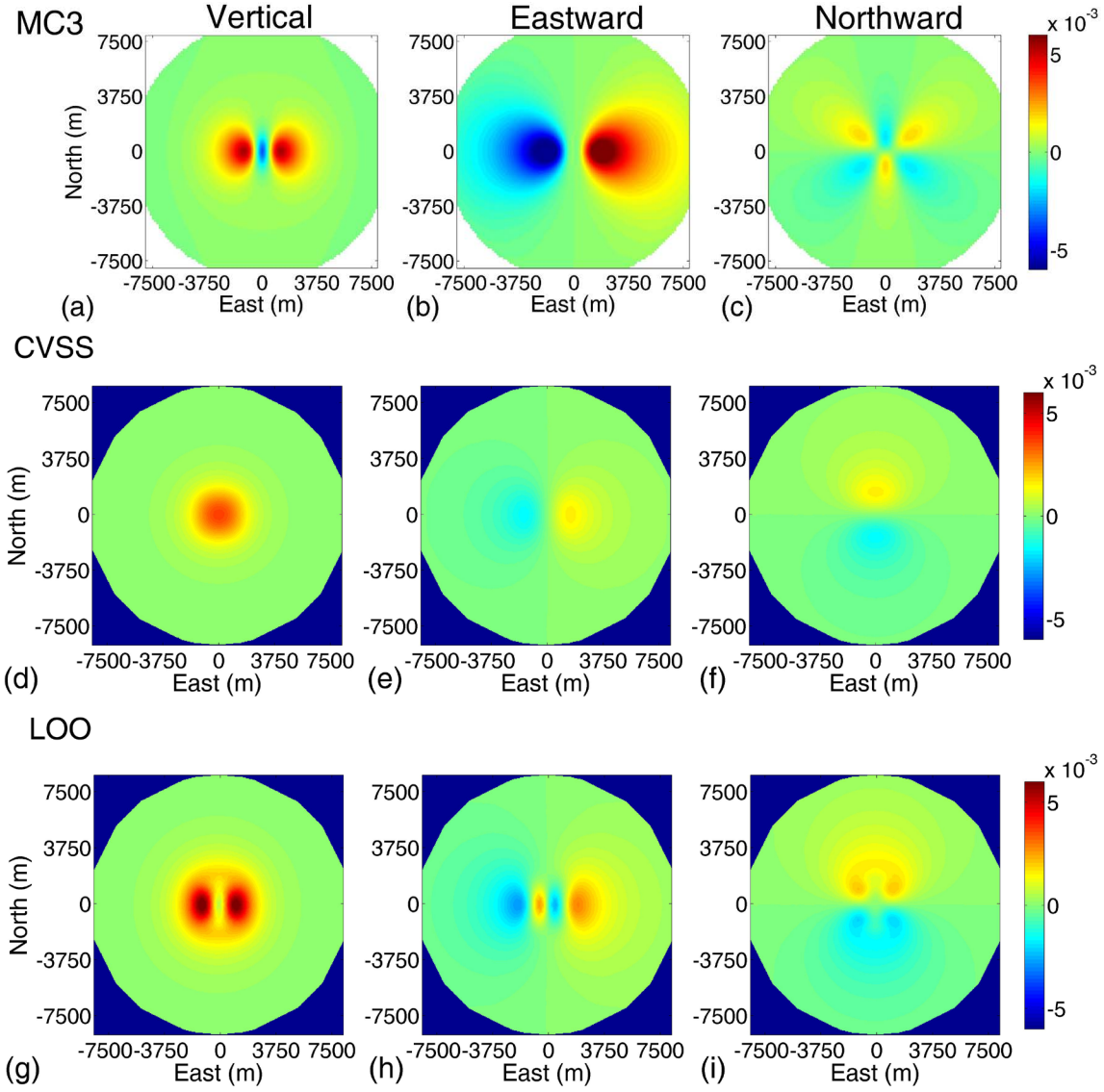

Figure 3-13. Displacements (m) produced by the best models for the extended grid inversion run to reproduce the vertical dike in the subsurface.
Images (a)-(c) show the MC3 vertical, eastward-westward, and northward-southward displacements respectively. Images (d)-(f) show the CVSS method best model's vertical, eastward-westward, and northward-southward displacements respectively. Images (g)-(i) show the LOO method best model's vertical, eastward-westward, and northward-southward displacements respectively.

The CVSS best model produced a reservoir-like source (Figure 3-14a), while the best LOO model produced a more complicated source volume distribution including both positive and negative volume changes (Figure 3-14b), which is appropriate for this grid because it includes points outside of the dike plane which will undergo negative volume changes during the dike opening.

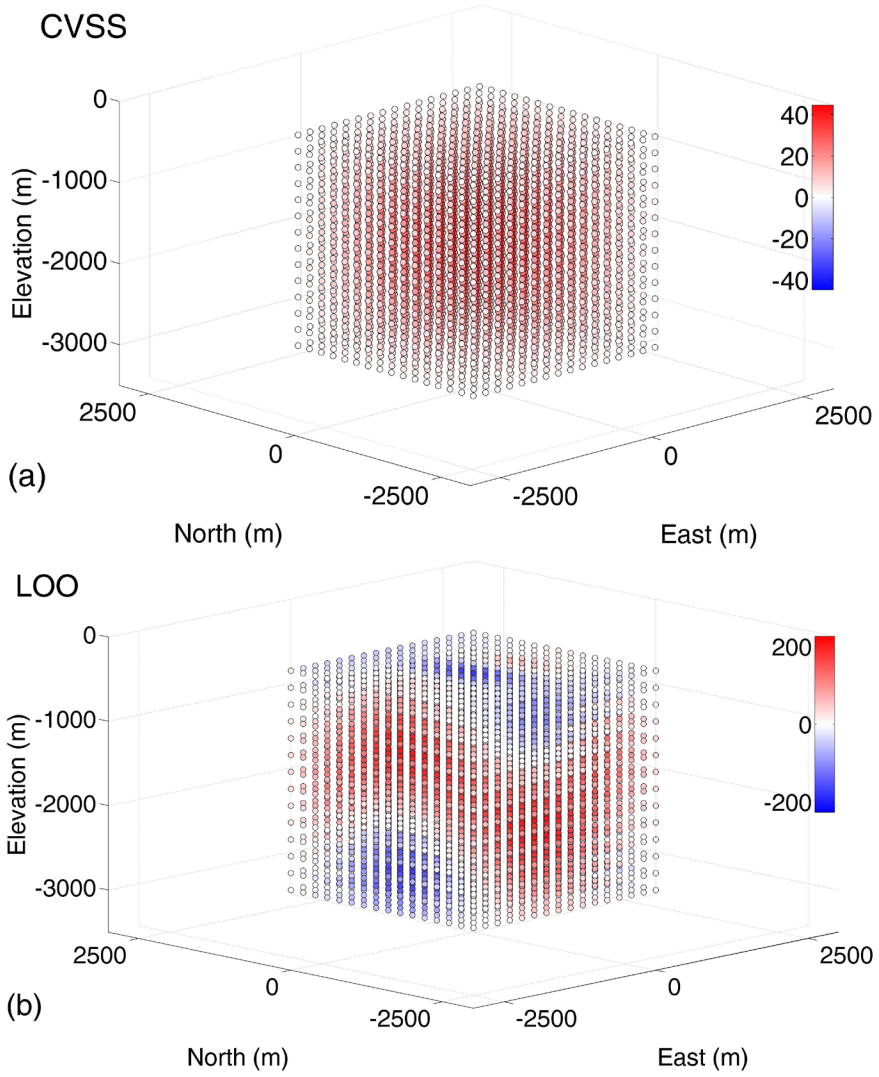

Figure 3-14. Full grid source volume distributions (m^3) for the best extended grid models for the vertical dike in the subsurface.
Image (a) shows the CVSS results and image (b) the LOO results.

We also focused on two specific planes in the grid to examine volume changes specifically where the dike plane is localized as well as on a plane (whose length is equal to one dike width) perpendicular to the center of the dike (Figure 3-15). The CVSS

method found a source volume distribution of solely dilating sources on these planes (Figure 3-15a,c). The sources within the space of the dike are undergoing a total volume change of $1x10^3$ m^3 (0.5% of the dike opening). The LOO method found areas of negative volume change at the top of the dike (Figure 3-15b), as well as at the top of the perpendicular plane (Figure 3-15d). The sources on the parallel plane are undergoing a total volume change of -167 m (-0.08% of the dike opening), which is of the wrong sign and order of magnitude for the actual opening of the dike, computed by MC3.

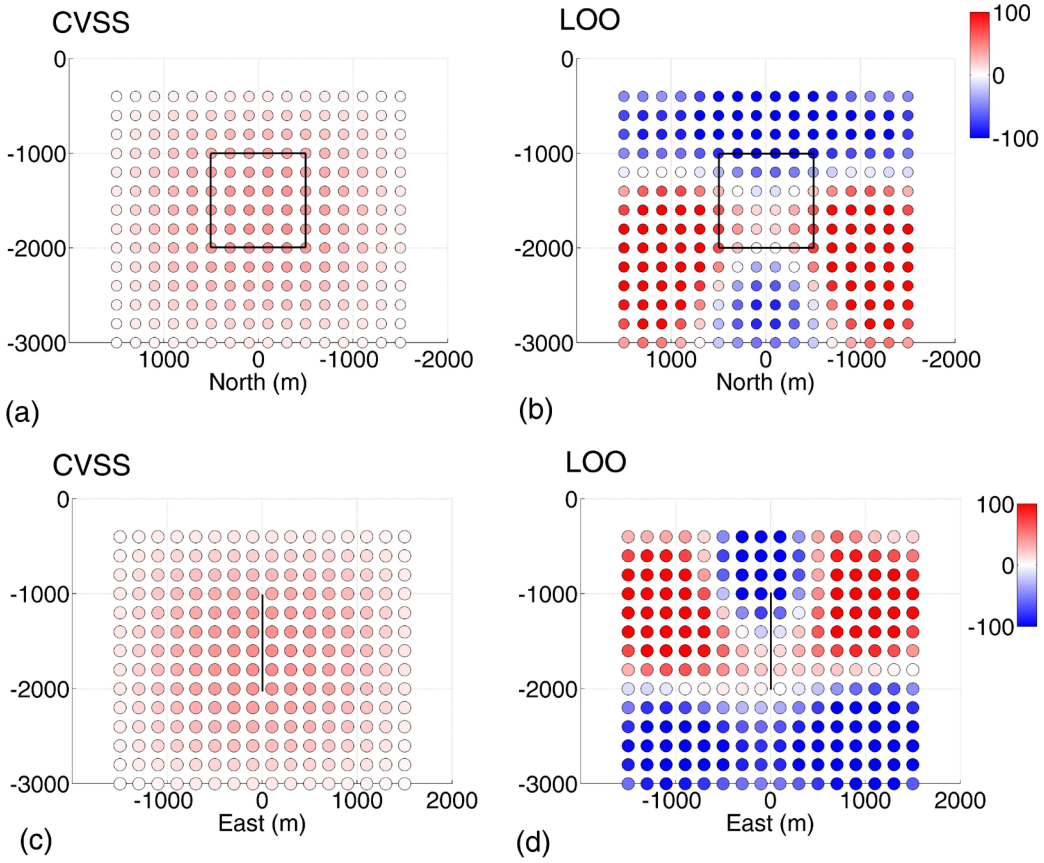

Figure 3-15. Source volume distributions (m^3) along the dike plane, and perpendicular to the dike plane, for the best extended grid models for the vertical dike in the subsurface.
Black square shows location of dike plane. Images (a) and (b) show the CVSS and LOO results, respectively, on the plane parallel to the dike and images (c) and (d) show the CVSS and LOO results, respectively, on the plane perpendicular to the center of the dike.

Using a plot produced by the software that shows the model misfit as a function of the number of sources taken into consideration in the calculation (Figure 3-16), we visually determined the minimum number of sources needed to keep the misfit low. This allows

us to minimize the model calculation time. Here we determined that 501 sources of our 3584 sources are sufficient.

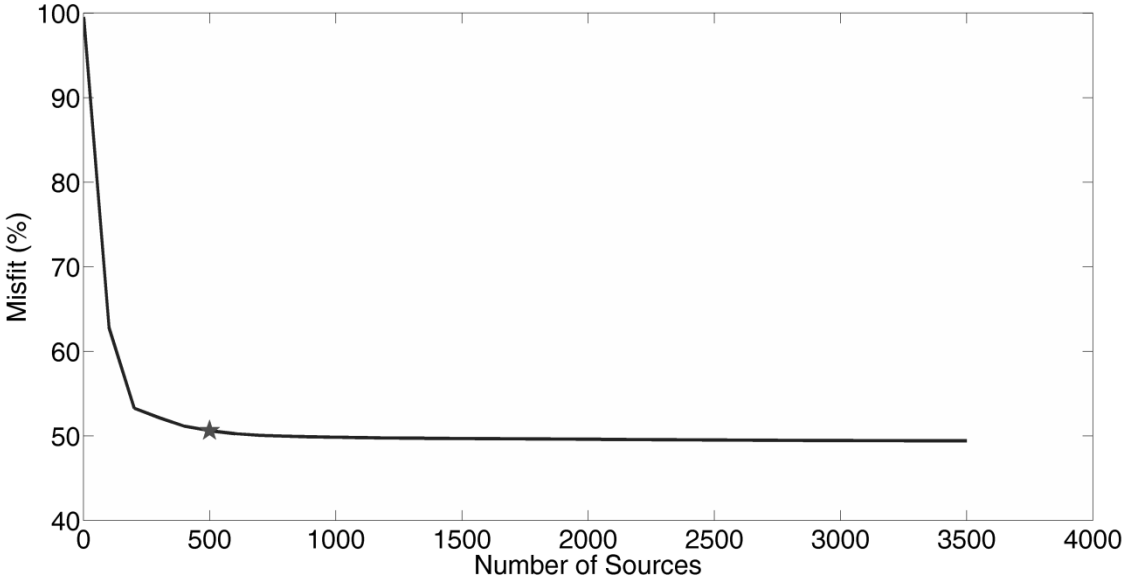

Figure 3-16. Plot of misfit versus number of sources included in the calculation for the best extended grid model for the vertical dike in the subsurface.
The star denotes where we visually identified the best compromise between number of sources (i.e., calculation time) and misfit.

The decimated source volume changes along the dike plane (Figure 3-17a) and a plane perpendicular to the center of the dike (Figure 3-17b) do focus in on the general area where the dike is localized. However, the sources within the dike space along the plane parallel to the dike are undergoing a total volume change of -40m^3 (-0.02% of the dike opening volume). This decimated source both fails to reproduce the expected sign of the volume changes along the dike plane (i.e., positive changes) and to reproduce the magnitude of the dike volume change.

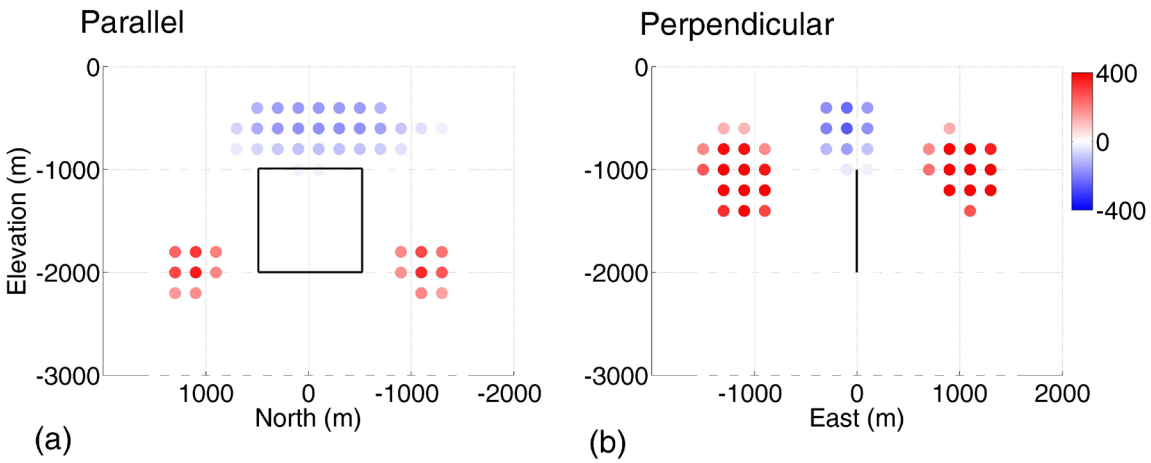

Figure 3-17. Decimated source volume distributions (m^3) along the dike plane, and on a plane perpendicular to the center dike plane, for the best extended grid model (LOO method) for the vertical dike in the subsurface.

Black square shows location of dike plane. Images (a) shows the results on the plane parallel to the dike and image (b) shows the results on the plane perpendicular to the center of the dike.

3.3.2. Non-vertical dike in the subsurface

For the non-vertical dike in the subsurface we only conducted an extended grid model due to limitations of the tomography toolbox, as discussed in Section 2.3.2. The best models determined by both the CVSS and LOO methods for this dike had higher $\log_{10}\rho^2$ values (Table 3-4) than any of the best models computed for the vertical dike in the subsurface. These models also had higher misfits than any of the vertical dike in the subsurface best models. Indeed, the misfits in all directions for the LOO model are nearly 100%. Further, both models underestimated the total volume change undergone during the dike opening by at least 50%.

Table 3-4. Results of tomography inversion models conducted to reproduce the non-vertical dike in the subsurface.

MODEL PARAMETERS		
Grid Shape	Extended	Extended
Cost Function	CVSS	LOO
Laplacian	Cross	Cross
$\rho^2(\log_{10})$	9.5	10.4
Volume Change (m^3)	$1x10^5$	$2x10^3$
MODEL MISFITS		
Overall (%)	67	98
Vertical (%)	62	98
Eastward-westward (%)	69	99
Northward-southward (%)	77	98
Volume changes retrieved (%)	50	1

The amplitude of the displacements computed by the LOO model are so low that the MC3 displacements cannot be plotted on the same color scale without severely distorting the MC3 displacement patterns. Therefore we plot the three models on a slightly exaggerated scale allowing at least the CVSS results to be seen (Figure 3-18). A separate exaggeration of the color scale for the LOO displacements shows they display the same pattern as the CVSS displacements, none of which match the MC3 results. However, it should be noted that displacements in all three directions are centered about one quarter dike width east of the central topography point (while displacements for the vertical dike

in the subsurface were centered at the central topography point, which is also the midpoint of the dike). We note this because this dike is not vertical and extends to the east. Nevertheless, we still see similar issues with this grid's displacement patterns as we saw with the point source grid models (i.e., an inability to reproduce the asymmetry in the displacement patterns; see Section 3.2.2). The displacement patterns for these models also show similar problems to the extended grid CVSS best model for the vertical dike in the subsurface (see Section 3.3.1.3). In particular, the vertical displacements form a bull's eye of uplift, with no associated subsidence. The eastward-westward displacements show the expected pattern of westward movement to the west of the north-south axis, and eastward movement to the east of this axis. Also, we see yet again northward-southward displacements missing the areas of movement directly north and south of the dike.

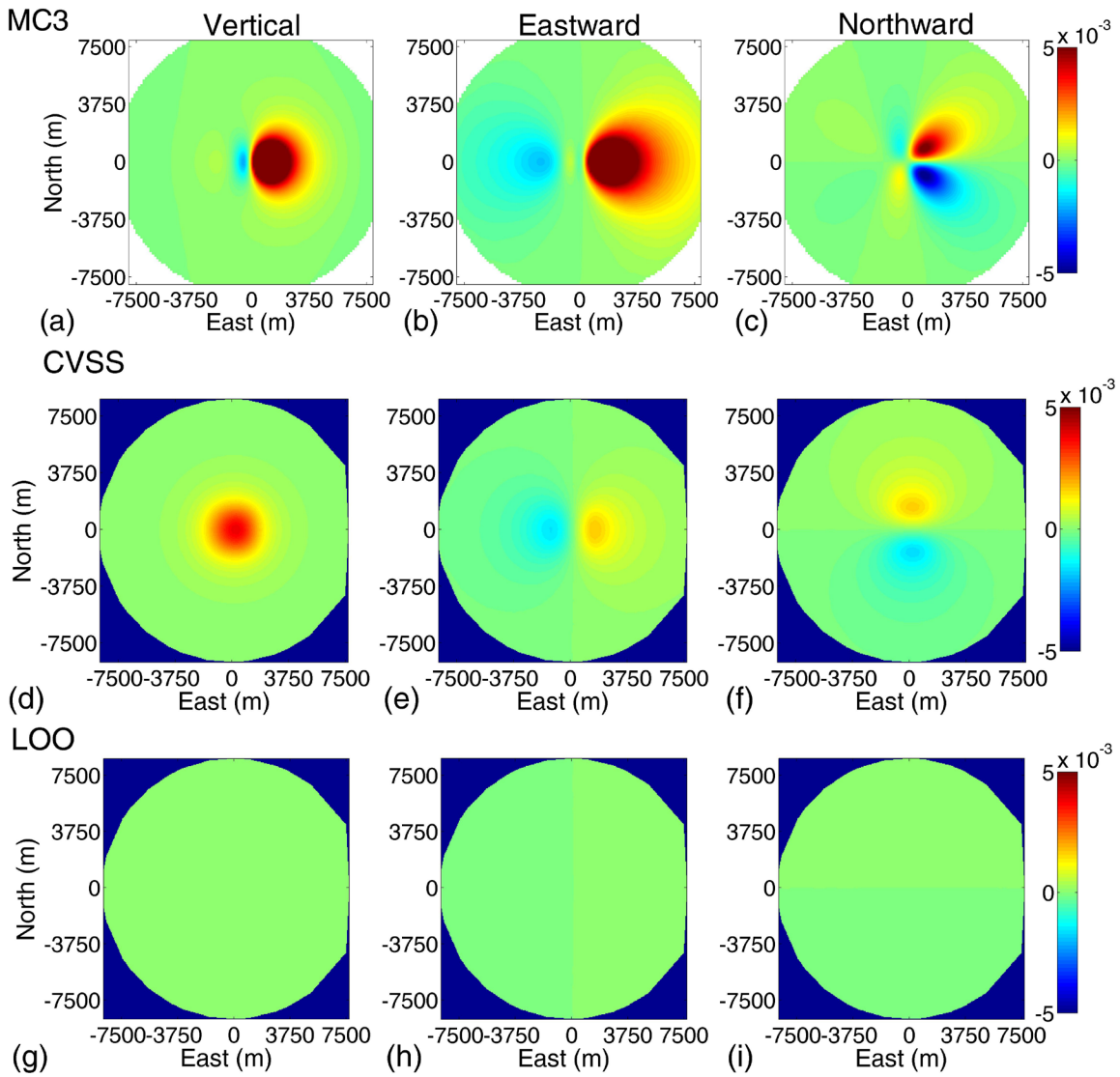

Figure 3-18. Displacements (m) produced by the best models for the extended grid inversion run to reproduce the non-vertical dike in the subsurface.
Images (a)-(c) show the MC3 vertical, eastward-westward, and northward-southward displacements respectively. Images (d)-(f) show the CVSS method best model's vertical, eastward-westward, and northward-southward displacements respectively. Images (g)-(i) show the LOO method best model's vertical, eastward-westward, and northward-southward displacements respectively.

Both of the best models produced reservoir-like sources (Figure 3-19) with weakly dilating sources, giving an overall volume change for both grids (Table 3-4) smaller than the MC3 computed dike opening volume (Table 3-1).

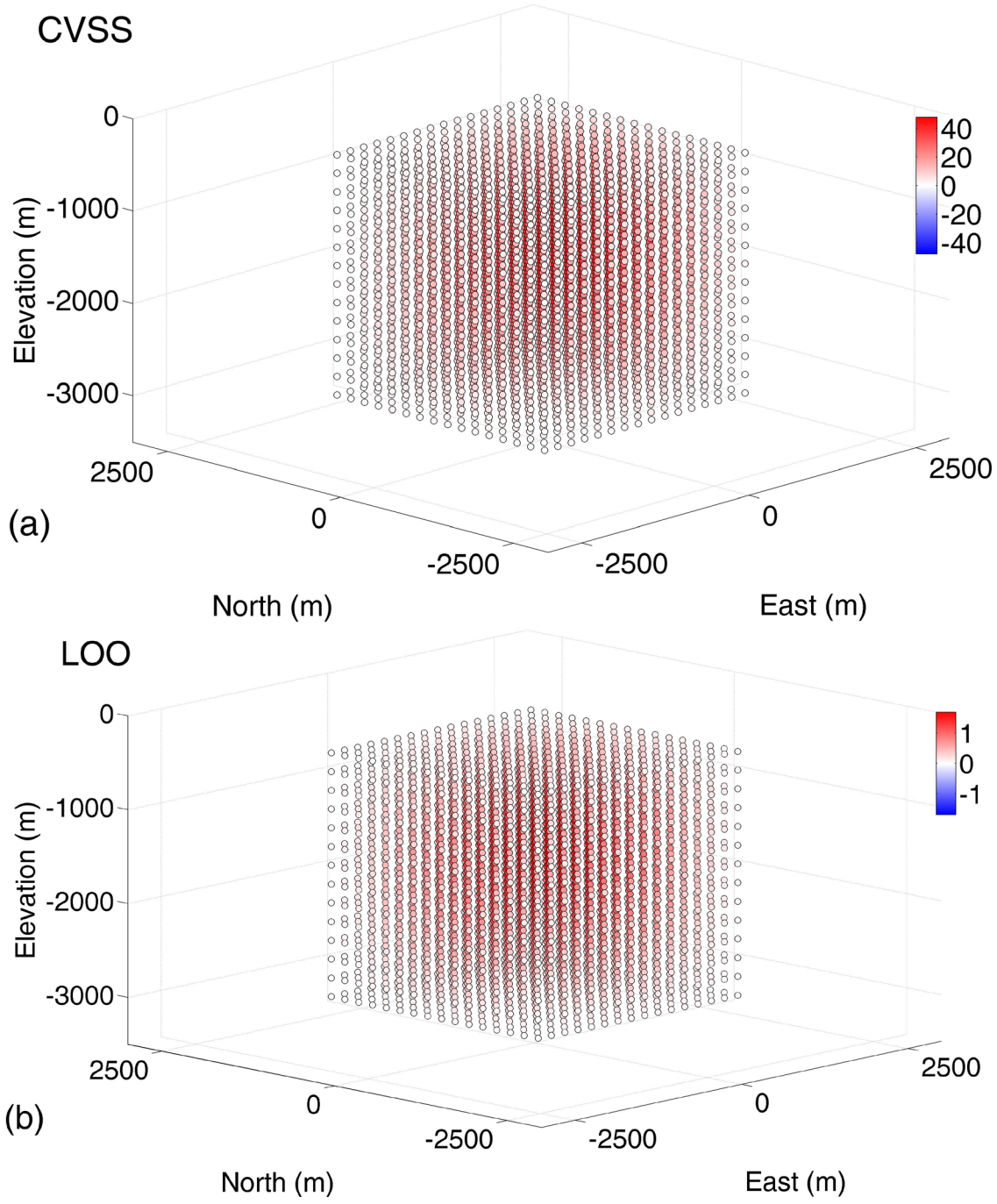

Figure 3-19. Source volume distributions (m^3) for the best extended grid models for the non-vertical dike in the subsurface.
Image (a) shows the CVSS results and image (b) the LOO results.

We also focused on two specific planes in the grid to examine volume changes on a plane parallel to the dike as well as on a plane perpendicular to the center of the dike (Figure

3-20). As seen in images (a) through (d), both methods found a source volume distribution of solely dilating sources. The CVSS sources within the dike space are undergoing a total volume change of $1.5x10^3$ m^3 (0.8% of the dike opening volume). The LOO sources in the dike space are undergoing a total volume change of 55 m^3 (0.03% of the dike opening volume). Ultimately, for this dike, the inversion technique was unable to reproduce the volume changes undergone by the dike, nor the displacements its opening induced.

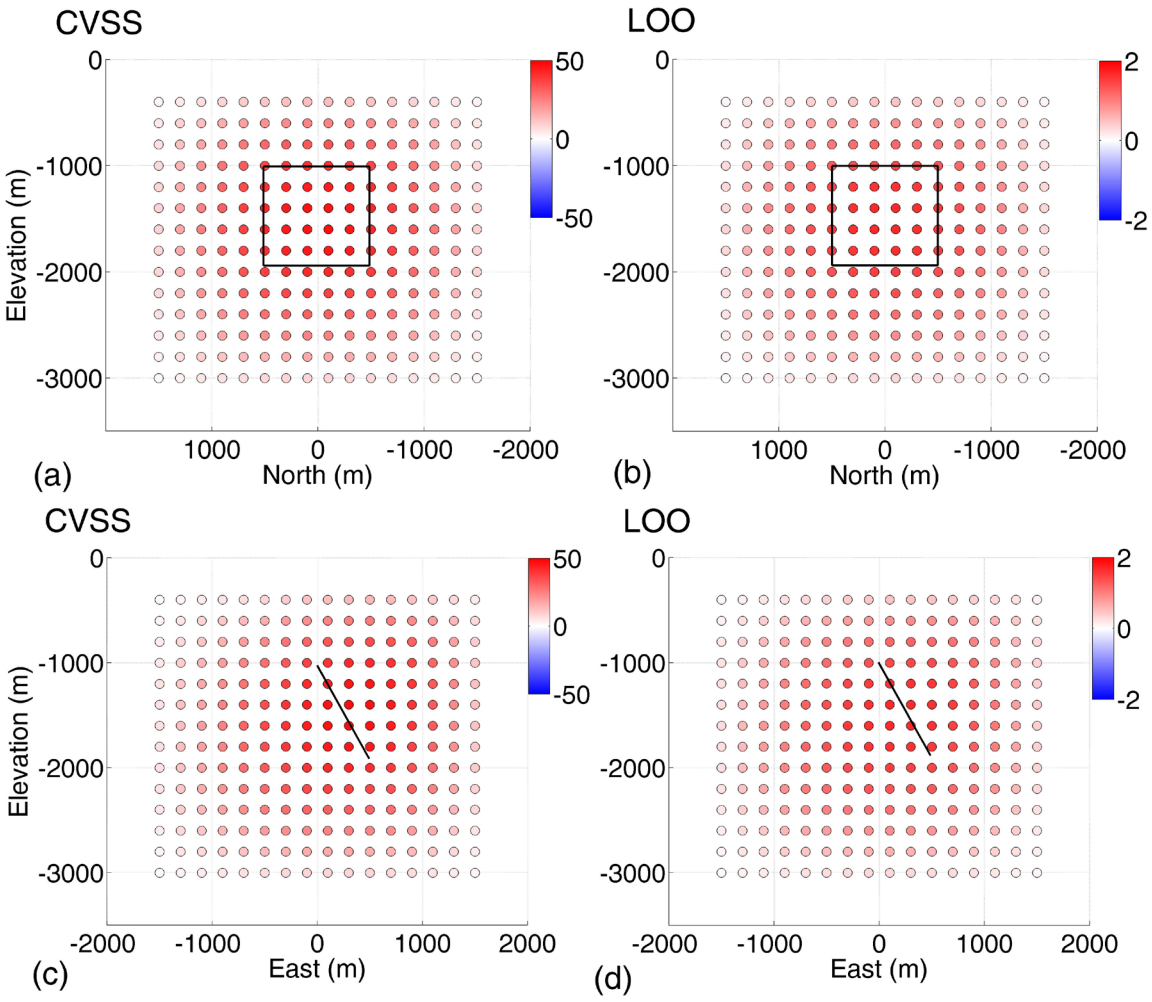

Figure 3-20. Source volume distributions (m^3) along the dike plane, and perpendicular to the dike plane, for the best extended grid models for the non-vertical dike in the subsurface.
Black square shows location of dike plane. Images (a) and (b) show the CVSS and LOO results, respectively, on the plane parallel to the dike and images (c) and (d) show the CVSS and LOO results, respectively, on the plane perpendicular to the center of the dike.

For this extended grid, we also attempted to focus on the most influential sources in the extended grid. Unlike with the vertical dike in the subsurface, the plot of model misfit as

a function of the number of sources taken into consideration in the calculation did not exhibit an exponential decay behavior. As seen in Figure 3-21, the misfit does not level out, and we need to include all of the sources to get the lowest possible misfit.

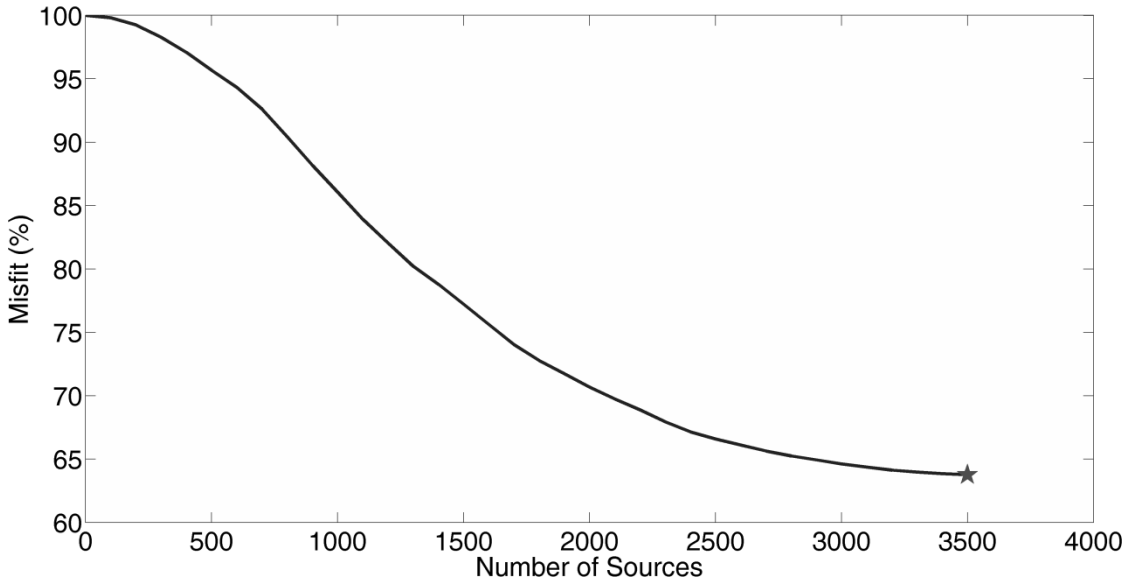

Figure 3-21. Plot of misfit versus number of sources included in the calculation for the best extended grid model for the non-vertical dike in the subsurface.
The star denotes where we visually identified the best compromise between number of sources (i.e., calculation time) and misfit.

3.3.3. Vertical dike reaching the ground surface

Overall, inversions conducted to characterize the vertical dike reaching the ground surface produced results similar to those for the other two dikes. We see many of the same problems with displacement patterns (Figure 3-22, Figure 3-24, Figure 3-26, Figure 3-28) as well as generally elevated misfits (Table 3-5). However, six of eight best models for this dike produced total volume changes on the same order of the dike opening as computed by MC3 (Table 3-1). The extended grid inversion for this dike produced the only best model among all nine inversions that overestimated the volume change.

Table 3-5. Results of tomography inversion models conducted to reproduce the vertical dike reaching the surface.

MODEL PARAMETERS								
MODEL	**1**	**1**	**2**	**2**	**3**	**3**	**4**	**4**
Grid Shape	1- plane	1- plane	3- plane	3- plane	3- plane	3- plane	Extended	Extended
Cost Function	CVSS	LOO	CVSS	LOO	CVSS	LOO	CVSS	LOO
Laplacian	N-S Plane	N-S Plane	Cross	Cross	N-S Plane	N-S Plane	Cross	Cross
ρ^2 (log_{10})	7.7	9.7	9.7	7.8	7.8	7.8	9.5	7.2
Volume Change (m^3)	$2x10^5$	$4x10^4$	$2x10^4$	$2x10^5$	$2x10^5$	$2x10^5$	$5x10^5$	$1x10^5$
MODEL MISFITS								
Overall (%)	38	74	85	43	38	38	93	51
Vertical (%)	31	35	57	69	60	60	72	61
Eastward-westward (%)	30	78	89	34	29	29	95	45
Northward-southward (%)	341	78	77	265	273	273	82	226
Volume changes retrieved (%)	67	13	7	67	67	67	167	33

3.3.3.1. Localized grid test - single plane grid

For these two models we see a large discrepancy in overall misfit, with the CVSS model having a misfit almost 40% lower than the LOO model. For both models, the vertical displacement misfit is reasonable and indeed the displacements produced (Figure 3-22d,g) do not completely match the MC3 displacement pattern, but their maximum values are at least of roughly the same order of magnitude as the MC3 result. The eastward-westward displacements show the expected overall pattern (Figure 3-22e,h), though displacements are not situated geographically where the MC3 results are. Further, the amplitude of the LOO results is too low. We see the same problem with the northward-southward displacement pattern as we have with every other model in this project. Further, the CVSS model for this grid has an extremely elevated northward-southward misfit, and we see in the results (Figure 3-22f) that these displacements have a much higher amplitude than the MC3 results. The LOO northward-southward displacements do not match the displacement pattern but are at least of roughly the same magnitude.

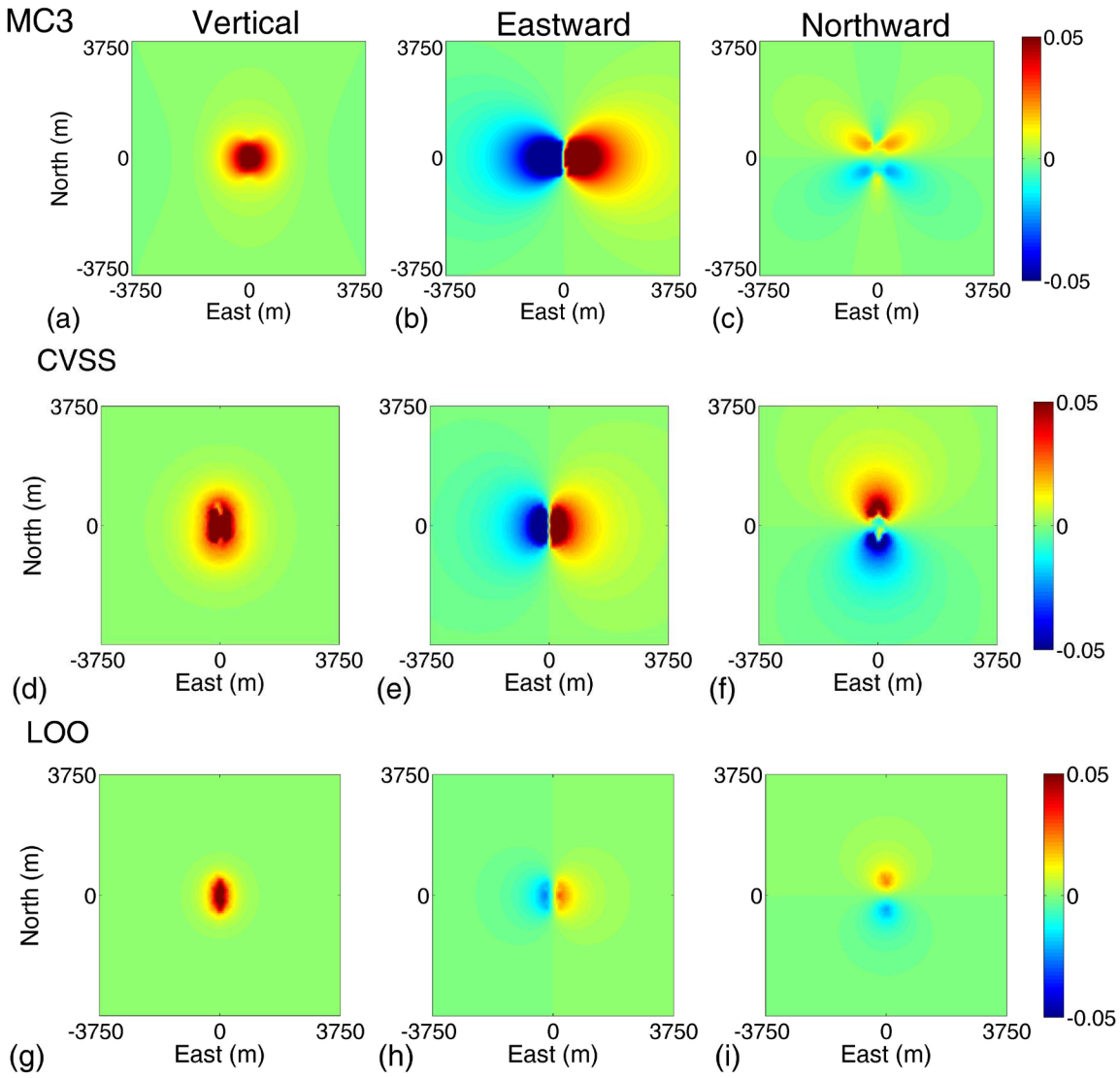

Figure 3-22. Displacements (m) produced by the best models for the single plane grid inversion run to reproduce the vertical dike rupturing at the ground surface.
Images (a)-(c) show the MC3 vertical, eastward-westward, and northward-southward displacements respectively. Images (d)-(f) show the CVSS method best model's vertical, eastward-westward, and northward-southward displacements respectively. Images (g)-(i) show the LOO method best model's vertical, eastward-westward, and northward-southward displacements respectively..

The $\log_{10}\rho^2$ values for the two best models differed by 2 units, with the LOO result being the smoother of the two. This can be seen in the source volume distributions retrieved (Figure 3-23). The LOO result includes only dilating sources, while the CVSS result incorporates negative sources as well. While the CVSS result's total volume change is close to that of the dike opening (Table 3-5), the roughness of this solution does not make

it feasible. The LOO result, while smooth, is an order of magnitude too low for the dike opening making this source also improbable.

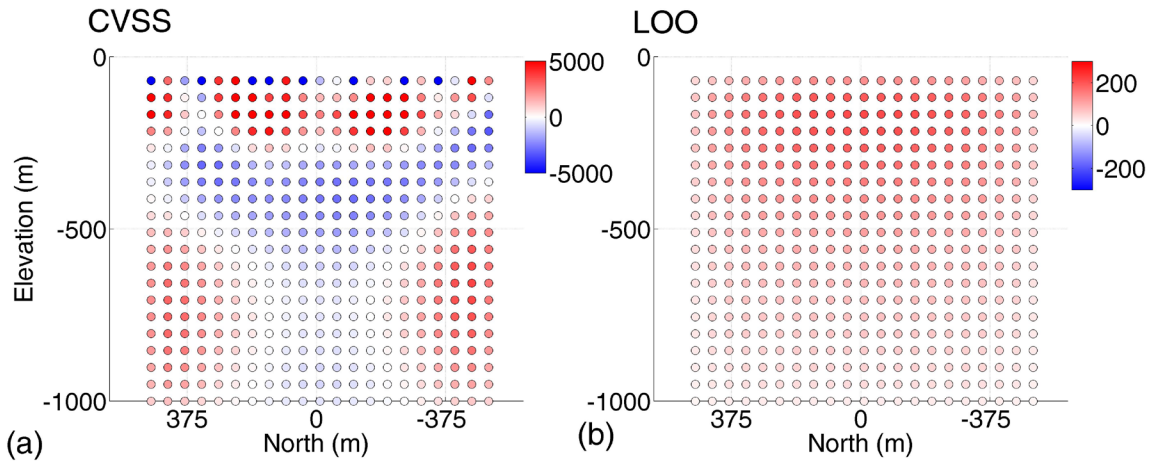

Figure 3-23. Source volume distributions (m^3) for the best single plane grid models for the vertical dike rupturing at the surface.
Image (a) shows the CVSS results and image (b) the LOO results.

3.3.3.2. Localized grid test - three plane grid

As with the vertical dike in the subsurface, for this dike we calculated two models using the two different Laplacian operators (see Figure 2-5). Using the 'cross' operator (i.e., the 3D operator), as with the vertical dike in the subsurface inversion, the two best models have different $\log_{10}\rho^2$ values, differing by about two units for this inversion. Unlike the vertical dike in the subsurface results for this grid, but similar to the single plane grid inversion for this dike, the misfits for the best models found for this inversion differ by about 40%, with the LOO method finding the model with the lower misfit.

The CVSS model's displacements (Figure 3-24d-f) have a much lower amplitude than the MC3 results, while the LOO results (Figure 3-24g-i) have a similar amplitude for the vertical and eastward-westward displacements. The LOO northward-southward displacements have a higher amplitude than the MC3 results, explaining their elevated misfit. Displacement patterns for both models show the same issues we saw with the single plane grid results, in particular the same problem with the northward-southward displacements we have seen in all of the models.

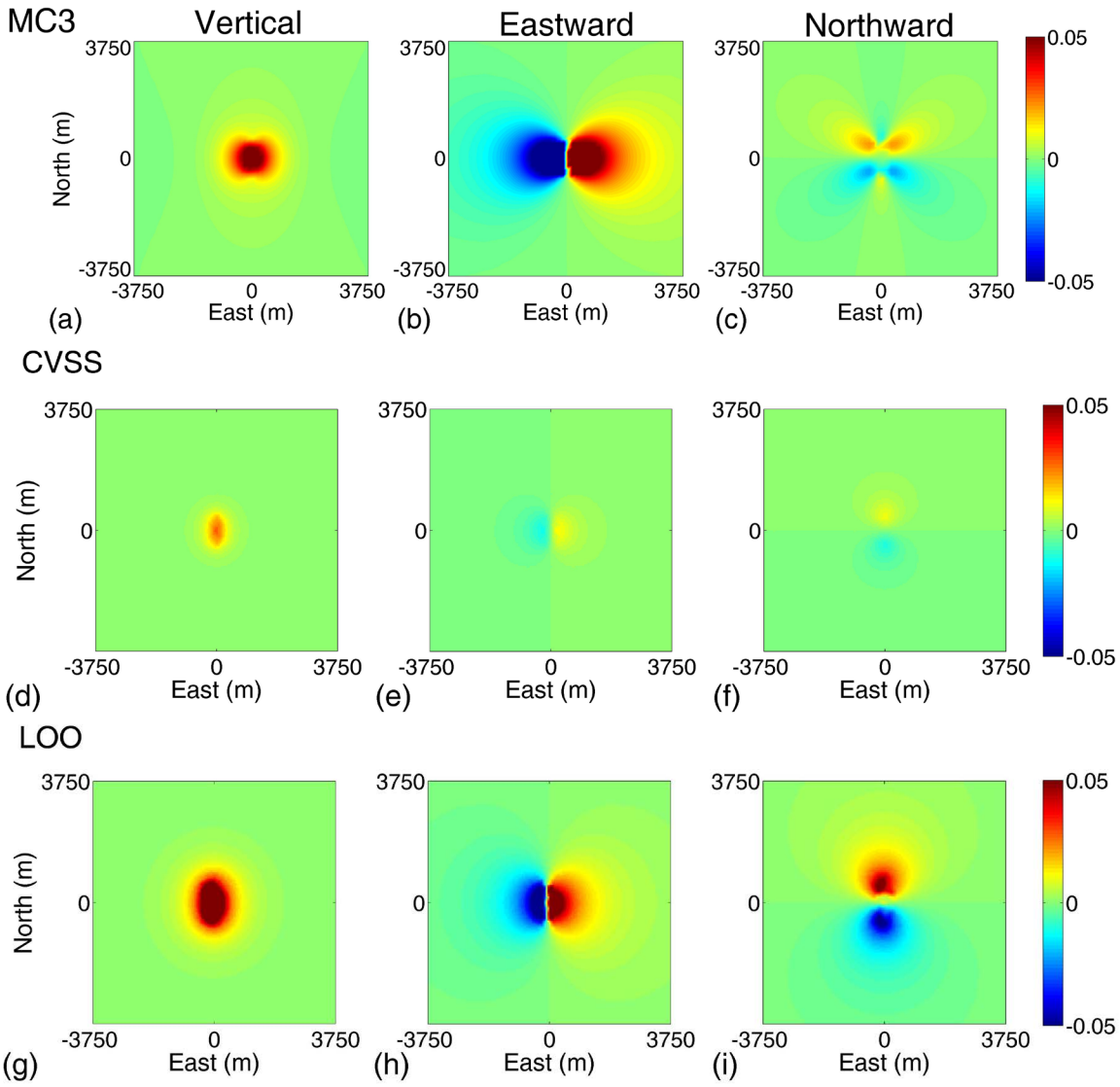

Figure 3-24. Displacements (m) produced by the best models, using the cross-shaped Laplacian, for three plane grid inversion run to reproduce the vertical dike reaching the ground surface.
Images (a)-(c) show the MC3 vertical, eastward-westward, and northward-southward displacements respectively. Images (d)-(f) show the CVSS method best model's vertical, eastward-westward, and northward-southward displacements respectively. Images (g)-(i) show the LOO method best model's vertical, eastward-westward, and northward-southward displacements respectively.

The source volume distribution retrieved by the CVSS model contains all dilating sources (Figure 3-25a), but the total volume change is an order of magnitude smaller than the dike opening. The LOO model reproduces the dike opening rather well (Table 3-5), but with a rough solution (Figure 3-25b). Therefore, both models ultimately do not produce viable sources.

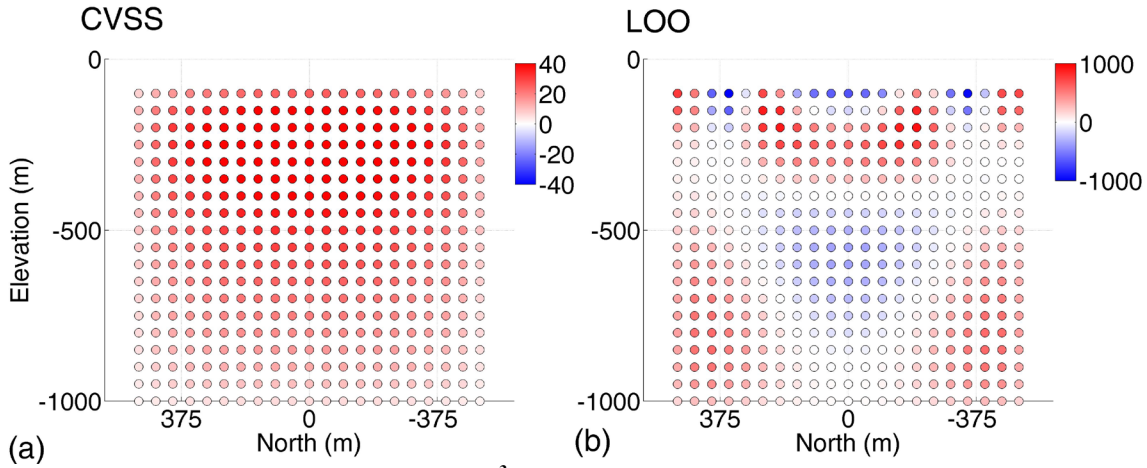

Figure 3-25. Source volume distributions (m^3) for the best three plane grid models, using the cross-shaped Laplacian, for the vertical dike rupturing at the surface.
Image (a) shows the CVSS results and image (b) the LOO results.

Using the north-south plane Laplacian operator (i.e., the 2D operator), both the CVSS and LOO methods found the same best model. In the previous two inversions, the models with the lowest misfits had a $\log_{10}\rho^2$ value similar to that for this best model. Indeed, this model has one of the lowest overall misfits found in any of the nine inversions, though with an elevated northward-southward misfit as we have seen in the other inversions for this dike. The displacement patterns for this dike (Figure 3-26) are similar to those found by the CVSS method's best model for the single plane inversion for this dike (Figure 3-22d-f) and the LOO method's best model for the three plane inversion using the 3D Laplacian (Figure 3-24g-i). Again, we have fundamental issues with the northward-southward displacements and vertical/eastward-westward displacements not covering the correct geographical extent. Displacement amplitudes for the vertical and eastward-westward displacements are similar to the MC3 results, but are too high for the northward-southward displacements.

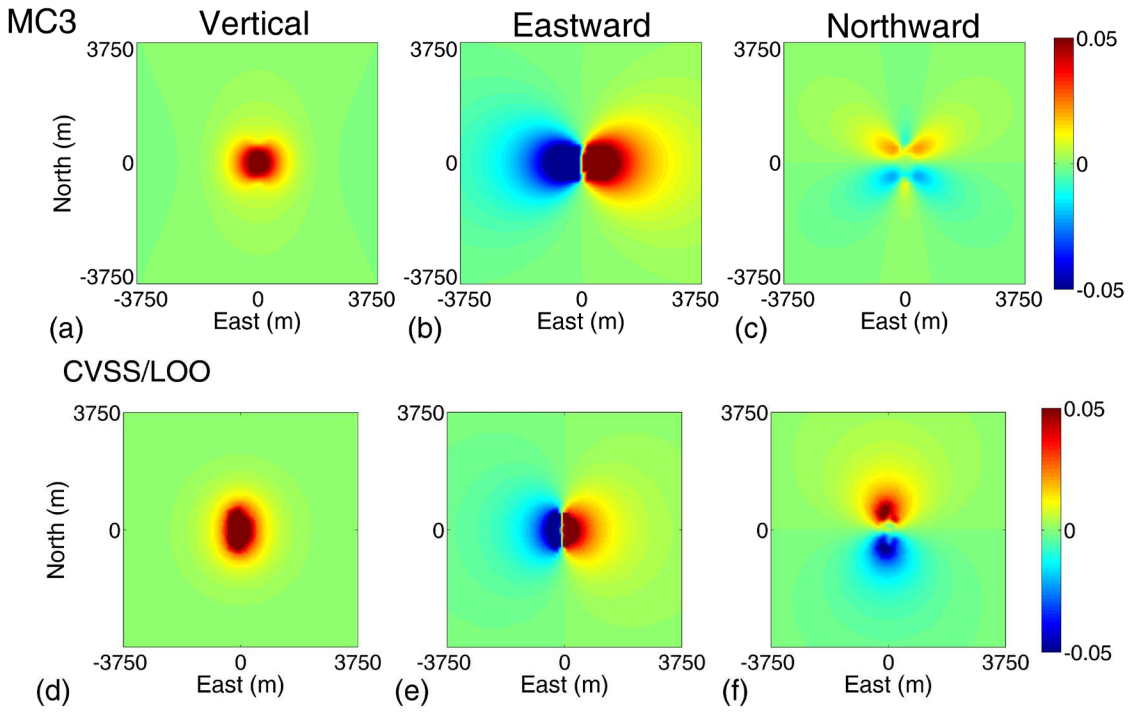

Figure 3-26. Displacements (m) produced by the best model, using the north-south plane Laplacian, for the three plane grid inversion run to reproduce the vertical dike reaching the ground surface. Images (a)-(c) show the MC3 vertical, eastward-westward, and northward-southward displacements respectively. The CVSS and LOO methods found the same best model for this grid; images (d)-(f) show this model's vertical, eastward-westward, and northward-southward displacements respectively.

The source volume distribution found for this model is relatively smooth, but includes some sources undergoing a negative volume change at the top of the grid (Figure 3-27). While this grid's volume changes reproduced 67% of the dike volume opening (Table 3-5), the presence of the negative sources makes this source improbable, as does its inability to reproduce the MC3 displacements.

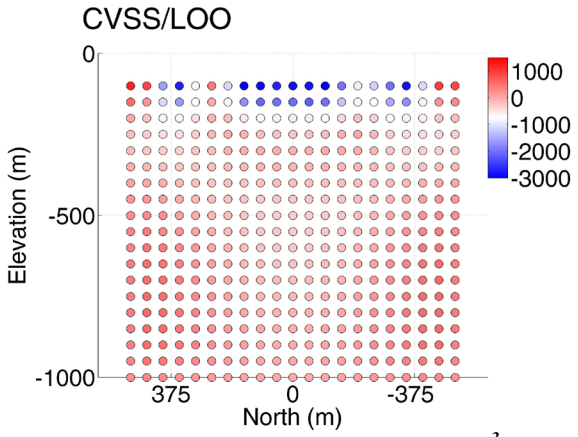

Figure 3-27. Source volume distribution (m^3) for the best three plane grid model, using the north-south plane Laplacian, for the vertical dike reaching the ground surface.

3.3.3.3. Extended grid test

For the extended grid test for the vertical dike reaching the ground surface, the best models have $\log_{10}\rho^2$ values similar to those found by other inversions for this dike. The CVSS method's best model had a $\log_{10}\rho^2$ value about two units higher than the LOO method's best model. The CVSS model also has an overall misfit about 40% higher than the LOO model's. As seen with the previous three inversions' best models with low overall misfits, while the LOO method found a model with a lower overall misfit, its northward-southward misfit is very high. Again, looking at the displacements (Figure 3-28) we can explain this with the discrepancy in northward-southward displacement amplitude. The CVSS displacements are barely visible when plotted using the same color scheme for all three models, while the LOO results are significantly higher than the MC3 results. For the other displacement directions, the CVSS displacements are too low, while the LOO displacements are of the right amplitude, but do not cover the same geographical extent as the MC3 results.

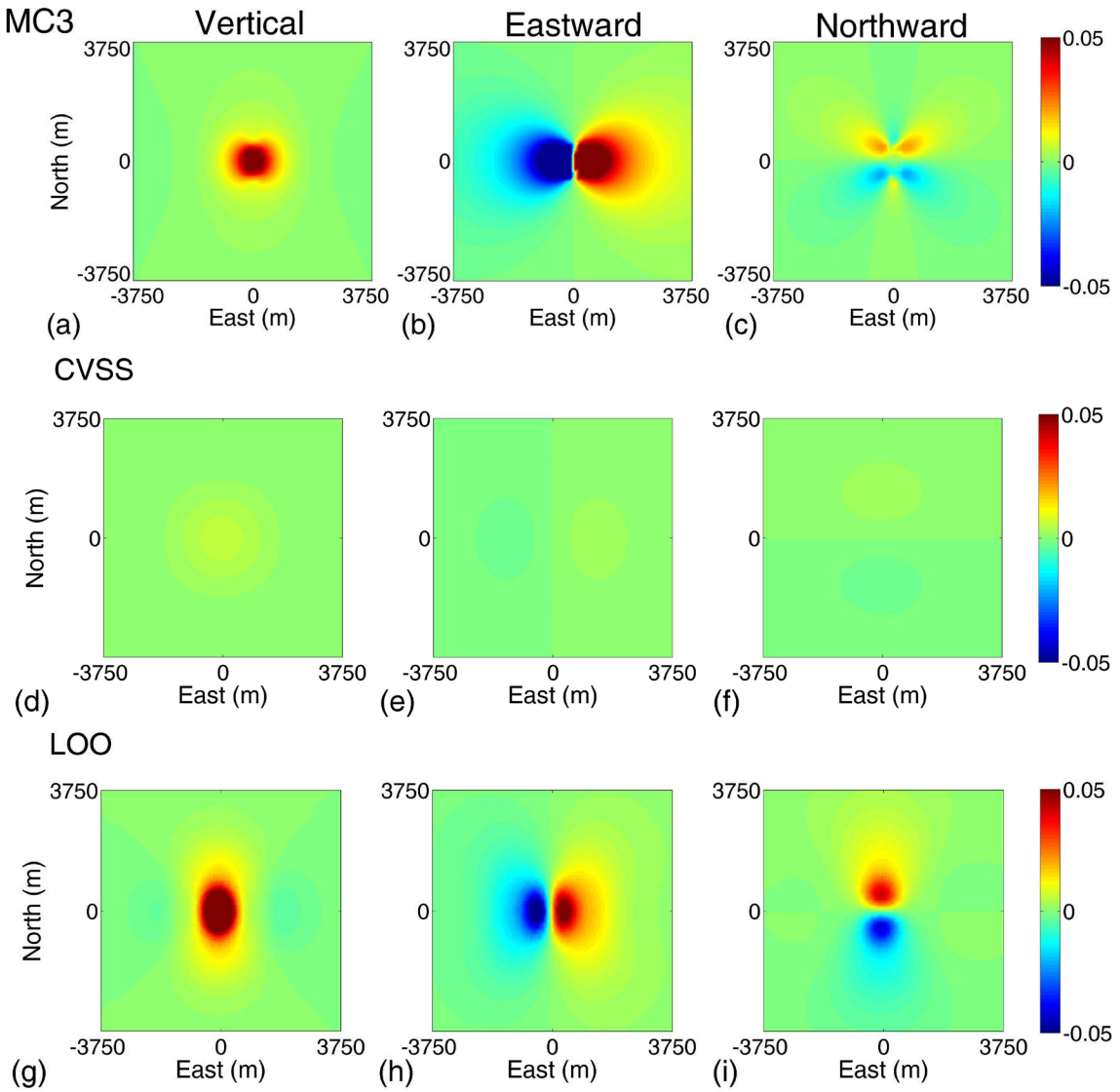

Figure 3-28. Displacements (m) produced by the best models for the extended grid inversion run to reproduce the vertical dike reaching the ground surface.
Images (a)-(c) show the MC3 vertical, eastward-westward, and northward-southward displacements respectively. Images (d)-(f) show the CVSS method best model's vertical, eastward-westward, and northward-southward displacements respectively. Images (g)-(i) show the LOO method best model's vertical, eastward-westward, and northward-southward displacements respectively.

As seen in both extended grid inversions for the other dikes, the CVSS model produced a reservoir-like source (Figure 3-29a). The LOO model produced more complicated sources for this dike (Figure 3-29b), with a central region undergoing positive volume changes, a ring of negative volume changes above and areas of negative volume changes to the southeast and southwest.

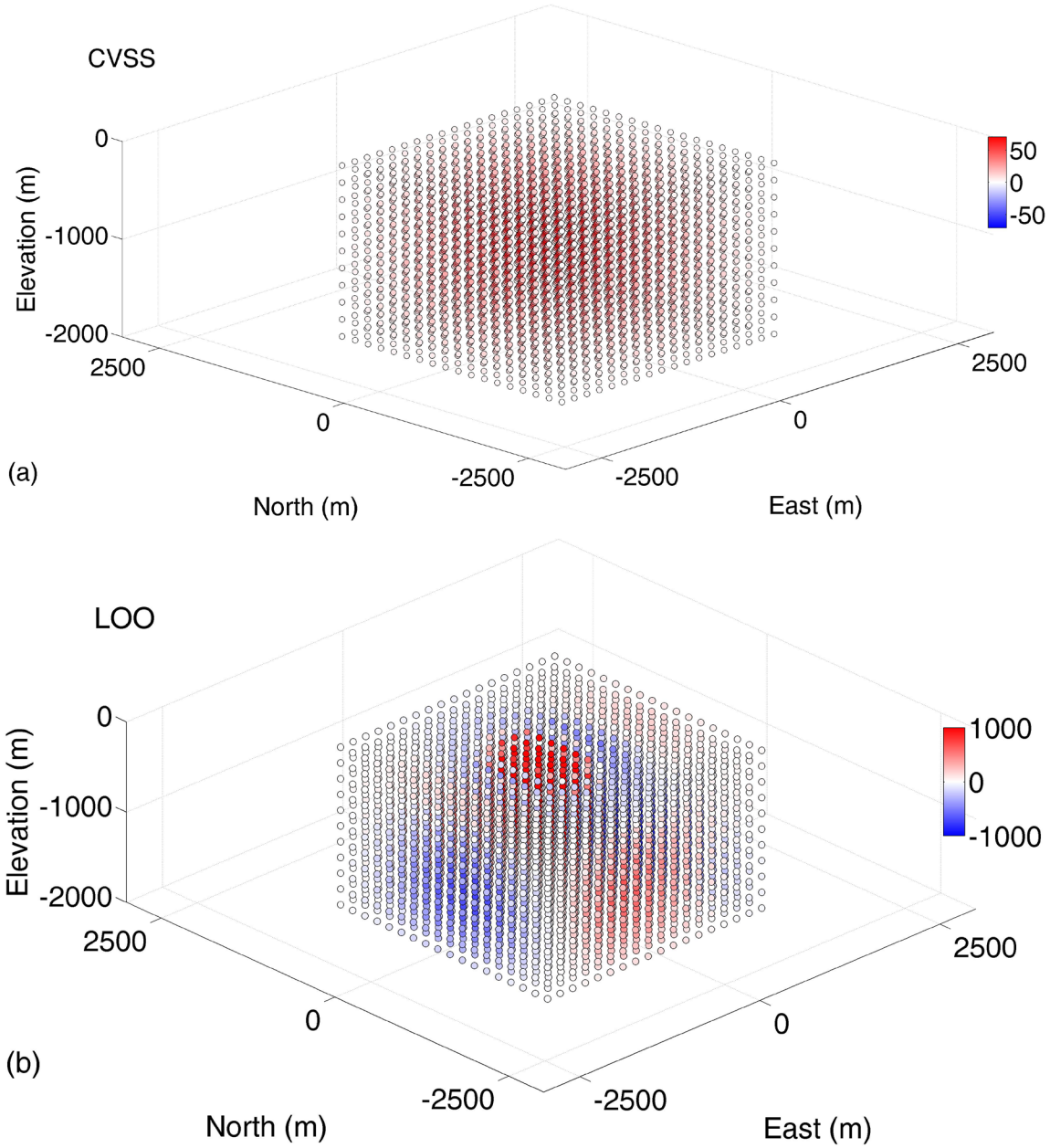

Figure 3-29. Source volume distributions (m^3) for the best extended grid models for the vertical dike rupturing at the surface.
Image (a) shows the CVSS results and image (b) the LOO results.

We also focused on two specific planes in the grid to examine volume changes specifically on a plane parallel to the dike, as well as on a plane perpendicular to the center of the dike (Figure 3-30). The CVSS model found only weakly inflating sources within the dike space undergoing a total volume change of about 960 m^3; this

corresponds to 0.3% of the dike opening volume. The LOO model found more strongly inflating sources on both planes, with some weakly negative sources on the perpendicular plane. The sources on the parallel plane are undergoing a $5x10^4$ m^3 volume change (17% of the dike opening). Both models are unable to reproduce the dike opening volume changes along the dike plane, as well as the correct patterns of displacements, making these retrieved sources improbable.

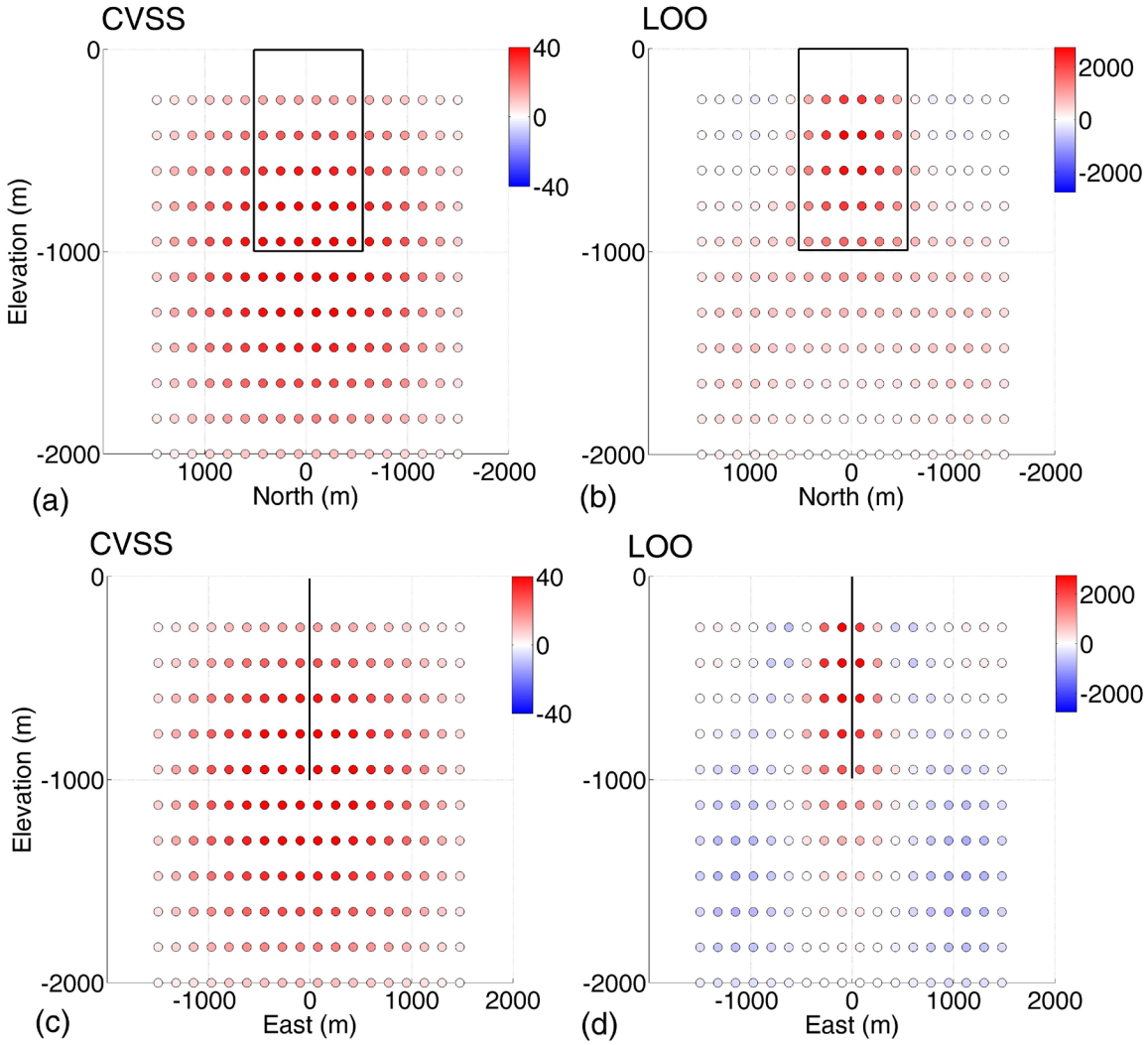

Figure 3-30. Source volume distributions (m^3) along the dike plane, and perpendicular to the dike plane, for the best extended grid models for the vertical dike reaching the ground subsurface. Black square shows location of dike plane. Images (a) and (b) show the CVSS and LOO results, respectively, on the plane parallel to the dike and images (c) and (d) show the CVSS and LOO results, respectively, on the plane perpendicular to the center of the dike

As with the vertical dike in the subsurface extended grid inversion, we used the tomography software to focus on the most influential sources in the extended grid. Using a plot that shows the model misfit as a function of the number of sources taken into consideration in the calculation (Figure 3-31), we visually determined we can keep the misfit low while minimizing the number of sources included in the calculation if we look at the 101 most influential sources.

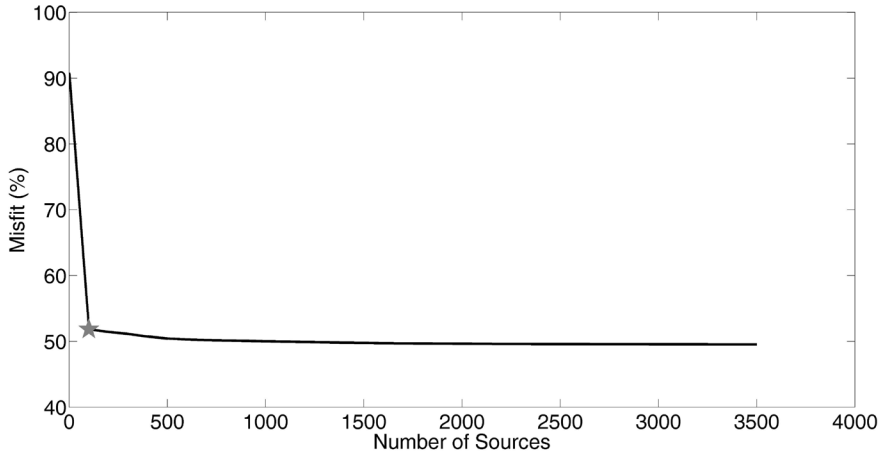

Figure 3-31. Plot of misfit versus number of sources included in the calculation for the best extended grid model for the vertical dike reaching the ground surface.
The star denotes where we visually identified the best compromise between number of sources (i.e., calculation time) and misfit.

As with the vertical dike in the subsurface, the decimated source focuses in on the general area where the dike is localized. However, along the dike plane the decimated source shows only inflating sources, while perpendicular to this plane we see positive sources near the dike, but some negative volume changes to the east and west (Figure 3-32). The sources along the plane parallel to the dike are undergoing a total volume change of $5x10^4$ m^3 (25% of the dike opening volume) while sources along the perpendicular plane are undergoing a total volume change of $3x10^4$ m^3 (15% of the dike opening volume). While the decimated source shows the expected sign for volume changes along the dike plane (i.e., positive changes), it fails to fully reproduce the dike volume change.

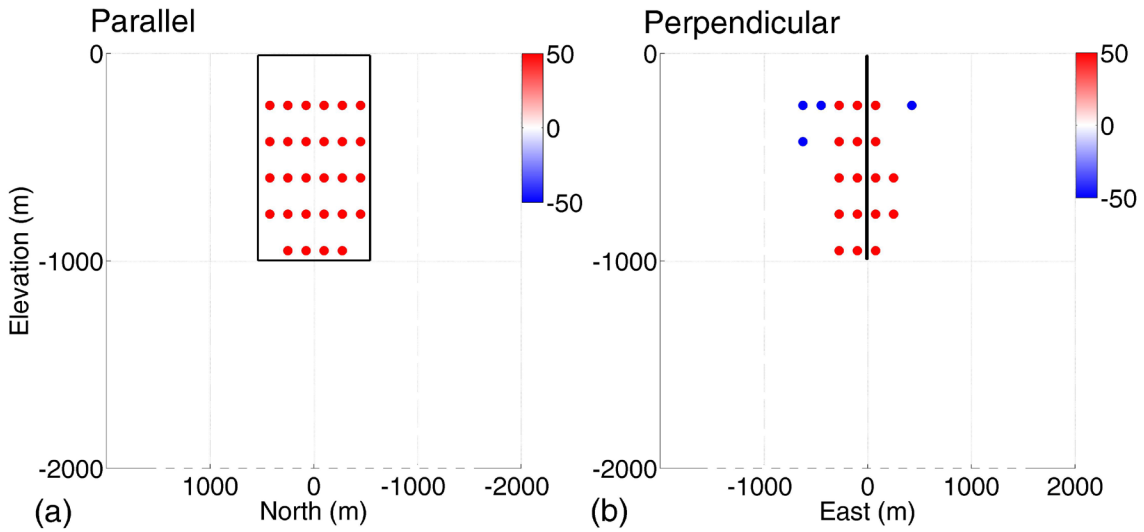

Figure 3-32. Decimated source volume distributions (m^3) along the dike plane, and perpendicular to the dike plane, for the best extended grid model (LOO method) for the vertical dike reaching the ground surface.
Black square shows location of dike plane. Images (a) shows the results on the plane parallel to the dike and image (b) shows the results on the plane perpendicular to the center of the dike.

3.3.4. Overall findings from the inversions

Across the board, the inversions did not reproduce the MC3 results well. Overall misfits ranged from 38% to 98%, with only two inversions producing 'best models' with misfits below 40%. Particularly high were the misfits for the northward-southward displacements, which for nearly every model were over 100%. The displacement maps produced by the inversions, as well as those produced by the point source grids, demonstrate a fundamental issue with using this tomography method for modeling fracture sources–point source grids do not produce the proper style of deformations for a fracture source.

Displacement patterns

Most noteworthy are the problems with the northward-southward displacement patterns. As with the point source grids, for all inversion results we see two main deformation features–northward movement north of the dike's center and southward movement south of the dike's center. We do not see the expected area of movement in the opposite directions directly north and south of the dike. As for vertical displacements, for the

vertical dike in the subsurface, the best models do show the bimodal deformation expected. For the other dikes, the vertical displacements are essentially 'bull's eyes' centered at the horizontal center of the dike, which is not the expected behavior seen with MC3. Finally, for eastward-westward displacements, we do see the expected eastward movement east of the dike and westward movement west of the dike, though for the best models for the vertical dike in the subsurface there are also small areas of movement in the opposite direction immediately adjacent to the north-south axis.

Also of note is the inability of the inversions to produce asymmetric displacements, as seen in the MC3 results for the non-vertical dike in the subsurface.

Best model determination

Looking across the models, the results do not seem to be affected by the method used for the best model determination. That is, neither the CVSS nor the LOO methods consistently produce models with lower misfits. Indeed, for the nine inversions, the lowest misfits were found with the LOO method in 5 models and by CVSS in 3. For one model, the two methods found the same best model. Further, among the nine inversions we do find instances where the roughness of the CVSS best model and that of the LOO best model are considerably different. However, we again do not see the LOO or CVSS methods consistently finding a rougher or smoother solution across the board. The CVSS result is smoother in five inversions and the LOO in three, with both methods finding the same best model for the ninth.

Laplacian operator effect

For the localized grid tests, we used two different Laplacian operators with the three plane grid inversions. For both the vertical dike in the subsurface and at the surface, the three plane grid inversions with the N-S plane operator had similar ρ^2 values. The misfits for the two best models for each dike using this operator are also similar for both the CVSS and LOO methods. In fact, for the vertical dike at the surface, both methods found the same best model. However, the two methods retrieved overall volume changes that differed by two orders of magnitude for the vertical dike in the subsurface. Comparing

the results from the N-S plane operator to those from the cross operator, for the vertical dike in the subsurface the misfits are similar across the board. For the vertical dike at the surface the misfits are similar except for the cross shaped operator CVSS best model which is significantly higher than the others.

Grid size

Very broadly, comparing the three grid types for the vertical dike models, the single plane grid produced the best model for the two vertical dikes (in terms of overall misfit), however the solution was also very rough for the vertical dike in the subsurface. The extended grids (which is what would be used when modeling with actual observations) all had misfits at nearly 50% or higher. All grids had fundamental issues producing the correct displacement patterns.

Volume changes

In terms of volume changes produced, the inversions attempting to find the vertical dike in the subsurface produced inconsistent overall volume changes, with values spanning two orders of magnitude among the eight 'best' models and with two best models producing negative total volume changes. Only three of the eight models produced positive volume changes in the entire grid tested on the same order of magnitude as the MC3 dike, but these results only retrieved 50% of the dike opening volume. For the non-vertical dike at depth, the best CVSS model produced volume changes on the same order of magnitude as the MC3 computed volume change (though it still only retrieved 50% of the dike opening volume), while the LOO result was two orders of magnitude lower. However, for the vertical dike reaching the ground surface, the inversions found volume changes that matched the order of magnitude of the MC3 dike rather well (i.e., in 6 of 8 'best' models), with four models retrieving 67% of the dike opening volume. One of these best models also overestimated the dike opening volume.

Looking qualitatively at the sign (i.e., negative or positive) of the volume changes found for our localized grids, we see negative sources included in the solution for all of the best models but two. As the fractures we are attempting to characterize are dilating sources,

we expect the entire dike to be opening (i.e., undergoing a positive volume change). For the extended grids none of the inversions found a plane of dilating sources in the location of the dike undergoing volume changes of the same magnitude as the opening dike. This held true even when we focused on only the most influential sources in the grid.

4. Discussion

4.1. Displacements patterns

Overall, the results of both the point source grid models and the tomography inversions indicate that displacement tomography cannot be used to retrieve source volume changes associated with the opening of a dike. Both techniques had trouble reproducing expected deformation patterns, particularly for northward-southward displacements. This ultimately leads back to the underlying deformation models. As seen in Equation (5), the displacement induced by each point source is going to essentially depend on its volume change and its distance from the ground surface point it is acting on. This calculation, designed to simulate a more reservoir-like source, is not going to be able to account for specificities of an opening fracture, which is characterized by continuity of stresses and displacement discontinuities across the fractures [*van Zwieten et al.*, 2013].

4.2. Volume changes

To further explore what is happening in the subsurface and better understand the volume changes produced by the inversion grids outside of the dike plane, we defined two planes in the subsurface for each dike and calculated stresses on these planes with MC3. The first was a plane parallel to the dike plane, extending one dike dimension beyond the dike edges to the north and south, as well as below the dike (and above the dike, for the dikes in the subsurface). The second plane was a plane perpendicular to the dike, situated at the center of the dike on the north-south axis. This plane extended one dike dimension beyond the dike plane to the east and west, and one dike dimension below the dike (and above the dike, for the dikes in the subsurface).

Immediately apparent in the results was that the volume changes in the surrounding rock computed by MC3 had a much smaller amplitude (by several orders of magnitude) than the volume changes retrieved by the extended grid inversions. For the vertical dike in the subsurface, on the plane parallel to the dike (Figure 4-1a-b), MC3 computes negative volume changes extending less than 100 m around the dike in all directions. Beyond these negative volume changes we see null values. The best LOO model did find some negative changes above and below the dike plane, including within the dike plane itself,

however also included some positive sources where we expect negative volume changes, and non-zero changes where we expect no changes. For the plane perpendicular to the dike (Figure 4-1c-d), MC3 computes negative volume changes above and below the dike. To the east and west of the dike are areas of increasing volume. The LOO model was able to reproduce negative volume changes above and below the dike plane with positive changes to the east and west, though the geographical extent of these volume changes do not completely align with those in the MC3 computations. Not shown here are the results of the best CVSS model which found only positive volume changes throughout the entire rock volume, not matching the expected volume changes on either plane.

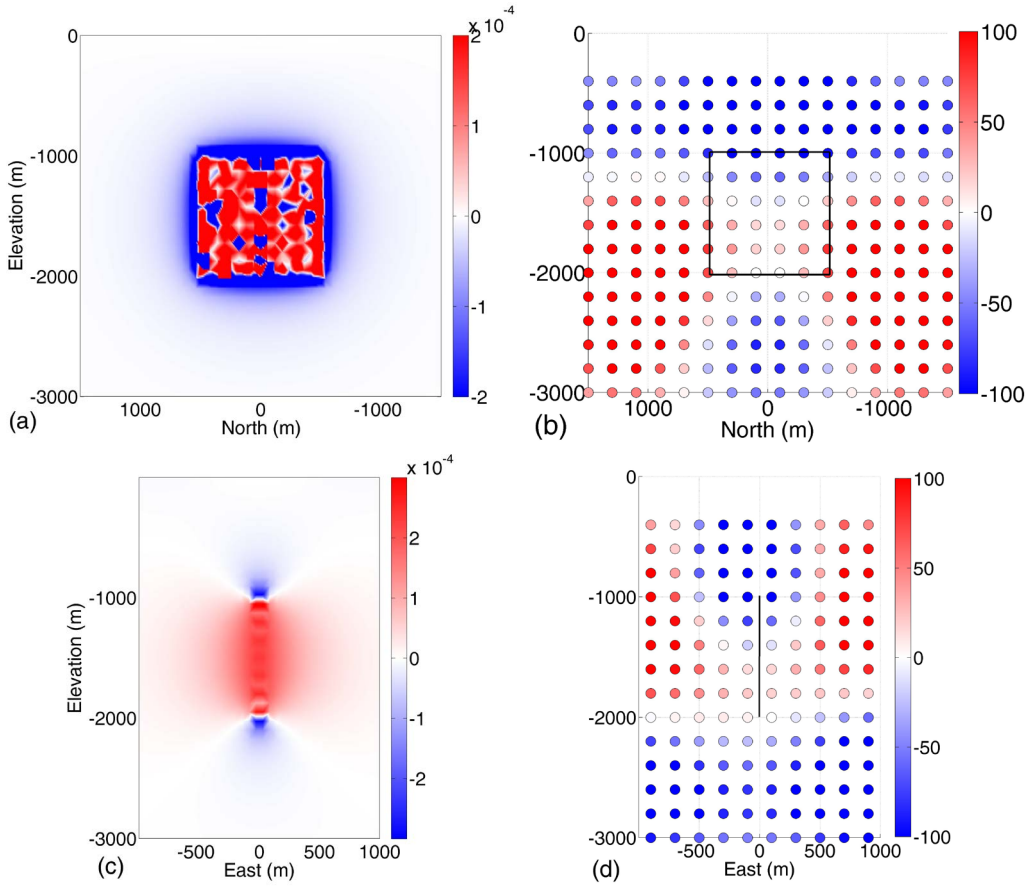

Figure 4-1. Volume changes (m^3) outside of the dike plane induced by the vertical dike in the subsurface and volume changes in the same space retrieved by the extended grid inversion.
Images (a)-(b) present volume changes on a north-south striking plane parallel to the dike plane. Image (a) shows the MC3 computations and image (b) shows results from the LOO best model found in the extended grid inversion. Images (c)-(d) present volume changes on an east-west striking plane perpendicular to the center of the dike plane. Image (c) shows the MC3 computations and image (d) the results from the LOO best model found in the extended grid inversion.

For the non-vertical dike in the subsurface, on the vertical plane parallel to the dike (Figure 4-2a-b), MC3 computes negative volume changes to the east and the west of the dike. Both of the best models for the extended grid inversion seeking to find this dike found only positive volume changes on this plane (results from the best LOO model are shown in the figure; volume change patterns were similar for the CVSS model, but maximum changes were an order of magnitude higher). For the vertical plane perpendicular to the dike (Figure 4-2c-d), MC3 computes negative volume changes above and below the dike. To the northeast and southwest of the dike are areas of increasing volume. Both of the best models for the extended grid inversion seeking to find this dike found only positive volume changes on this plane. Neither models from the inversion were able to reproduce the MC3 volume changes computed on these two planes.

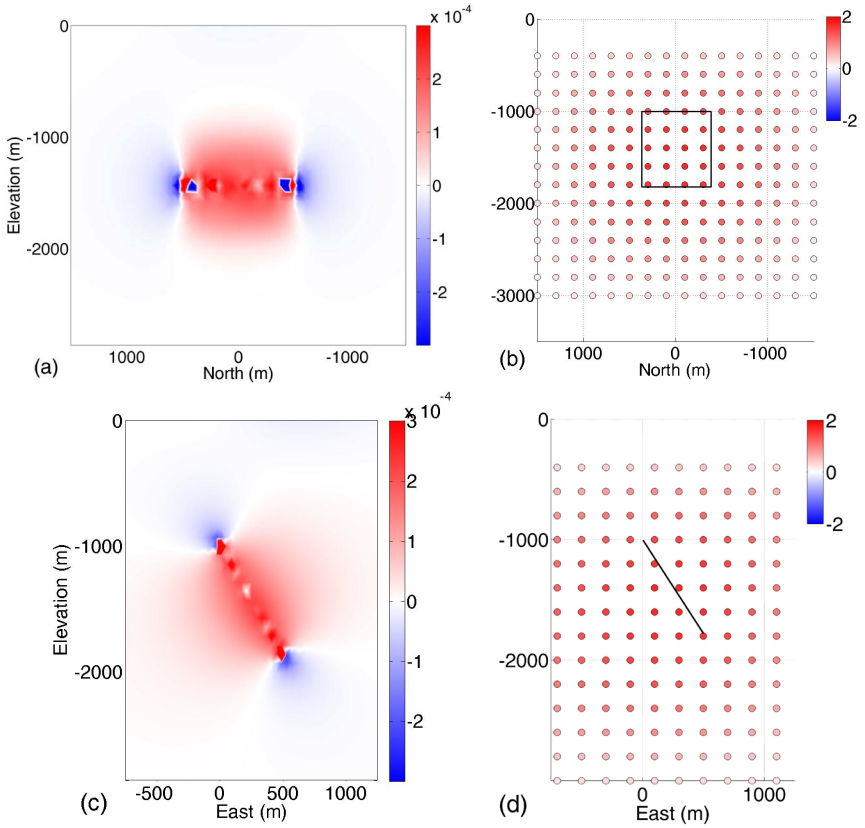

Figure 4-2. Volume changes (m^3) outside of the dike plane for the non-vertical dike in the subsurface and volume changes in the same space retrieved by the extended grid inversion.
Images (a)-(b) present volume changes on a vertical plane parallel to the dike plane. Image (a) shows the MC3 computations and image (b) shows results from the LOO best model found in the extended grid inversion for this dike. Images (c)-(d) present volume changes on an east-west striking vertical plane perpendicular to the center of the dike plane. Image (c) shows the MC3 computations and image (d) results from the LOO best model found in the extended grid inversion for this dike.

For the vertical dike reaching the ground surface, on the plane parallel to the dike (Figure 4-3a-b), MC3 computes negative volume changes surrounding the dike in all directions which then approach zero as we move away from the dike. The best LOO model found mostly positive volume changes with areas of weakly negative volume changes at the top northern and southern corners of the plane. For the plane perpendicular to the dike (Figure 4-3c-d), MC3 computes negative volume changes below the dike with increasing volume to the east and west of the dike. The LOO model found positive volume changes below the dike as well as about half a dike width to the east and west of the dike. To the east and west of these areas of positive volume changes are areas of negative volume changes. Not shown here are the results of the best CVSS model which found only positive volume changes throughout the entire rock volume, not matching the expected volume changes on either plane. Neither of these models were able to reproduce the MC3 computed volume changes on this plane.

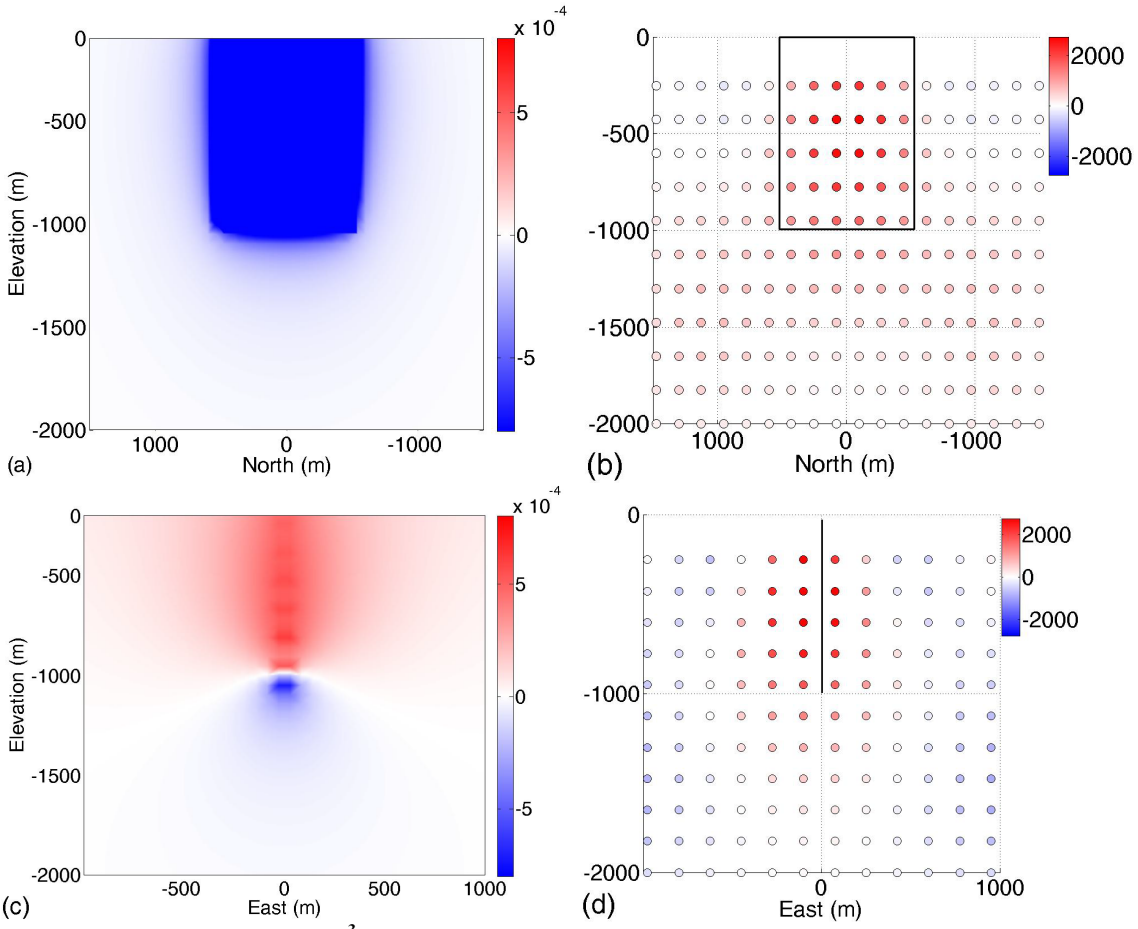

Figure 4-3. Volume changes (m^3) outside of the dike plane for the vertical dike reaching the ground surface and volume changes in the same space retrieved by the extended grid inversion.
Images (a)-(b) present volume changes on a north-south striking plane parallel to the dike plane. Image (a) shows the MC3 computations and image (b) shows results from the LOO best model found in the extended grid inversion. Images (c)-(d) present volume changes on an east-west striking plane perpendicular to the center of the dike plane. Image (c) shows the MC3 computations and image (d) shows results from the LOO best model found in the extended grid inversion.

While none of the extended grid inversions reproduced the expected volume changes outside the dike plane, we can see symmetric features in the volume change patterns from the LOO best results for both vertical dike models. These features are centered around the general location of the dike and could allow us to zoom in on the general location of the source even though not locating it perfectly.

5. Conclusions

For the tomography technique to be a viable method for modeling fracture sources, the underlying deformation model (i.e., point sources undergoing a volume change) needs to be able to reproduce the style and magnitude of deformations resulting from fracture sources. However, by testing grids of point sources in the same location and with the same volume variations as the dike elements as well as various inversions, we were unable to reproduce the displacements produced by an established fracture source model (MC3), particularly for northward-southward displacements.

Also of interest is the tomography method's ability to accurately reproduce the volume changes undergone by the source and within the surrounding rock. In the case of the vertical dike reaching the ground surface, we see relatively consistent volume changes (in terms of order of magnitude) found by all inversions; these inversions retrieved, on average, 61% of the dike volume change. For the other dikes, the results were less consistent. On average, the vertical dike in the subsurface inversions retrieved -12% of the dike volume changes while the non-vertical dike in the subsurface inversions retrieved 26% of the volume changes. One of the two non-vertical dike in the subsurface results matched the order of magnitude of the MC3 results and only three of the eight best models for the vertical dike in the subsurface matched the order of magnitude of the MC3 results (with the correct sign).

When comparing volume changes in the extended grid to those expected in the space around an opening dike we also found the tomography model was not able to reproduce volume changes associated with a sheet intrusion. However, if we look at general patterns in these results, as well as the decimated source volume distribution for the full grids, we may be able to hone in on the location of the dike, though would first need to make an assumption as to whether the deformation source is a dike or reservoir. Using observed vertical and horizontal displacements it can be possible to distinguish between displacements induced by fractures as opposed to 'more equidimensional magma bodies' [e.g., *Segall*, 2010, pp. 229-230]. If our observed surface deformations suggest the presence of a reservoir, we can safely switch to the tomography method, while if the

deformations suggest the presence of a dike we could then attempt to use tomography results to better inform a more computationally intensive model (such as an NA-MBEM) without adding additional assumptions to the inputs.

Ultimately, while the tomography inversions of extended source grids produce some potentially useful information via volume changes outside the dike plane and the decimated source grids, overall the results of this project indicate that the deformation model used in the tomography inversions is not appropriate for fracture sources. To make displacement tomography more appropriate for fracture sources, Green's functions for fracture sources would somehow need to be adopted to use in a grid of sources. Further, modeling actual fractures can be more complicated as they are not isotropic and the orientation of the plane must be described. An overview of existing solutions is provided in *van Zwieten et al.* [2013].

6. References

Amelung, F., S. Jonsson, H. Zebker, and P. Segall (2000), Widespread uplift and 'trapdoor' faulting on Galapagos volcanoes observed with radar interferometry, *Nature*, *407*(6807), 993-996.

Augier, A. (2012), Étude de l'éruption d'avril 2007 du Piton de la Fournaise (île de La Réunion) à partir de données d'interférométrie RADAR et GPS, développement et application de procédures de modélisation, 300 pp, Université Blaise Pascal, Clermont-Ferrand, France.

Cayol, V., and F. H. Cornet (1997), 3D mixed boundary elements for elastostatic deformation field analysis, *International Journal of Rock Mechanics and Mining Sciences*, *34*(2), 275-287.

Crouch, S. L. (1976), Solution of plane elasticity problems by the displacement discontinuity method, *International Journal for Numerical Methods in Engineering*, *10*(2), 301-343.

Davis, P. M. (1986), Surface deformation due to inflation of an arbitrarily oriented triaxial ellipsoidal cavity in an elastic half-space, with reference to Kilauea volcano, Hawaii, *Journal of Geophysical Research: Solid Earth*, *91*(B7), 7429-7438.

Dieterich, J. H., and R. W. Decker (1975), Finite element modeling of surface deformation associated with volcanism, *Journal of Geophysical Research*, *80*(29), 4094-4102.

Dixon, T. H., A. Mao, M. Bursik, M. Heflin, J. Langbein, R. Stein, and F. Webb (1997), Continuous monitoring of surface deformation at Long Valley Caldera, California, with GPS, *Journal of Geophysical Research: Solid Earth*, *102*(B6), 12017-12034.

Dzurisin, D. (1992), Electronic tiltmeters for volcano monitoring: lessons from Mount St. Helens, in *Monitoring volcanoes: techniques and strategies used by the staff of the Cascades Volcano Observatory, 1980-90*, U.S. Geological Survey Bulletin 1966, edited by J.W. Ewert and D.A Swanson, pp. 69-74, United States Government Printing Office, Washington DC.

Dzurisin, D. (2003), A comprehensive approach to monitoring volcano deformation as a window on the eruption cycle, *Reviews of Geophysics*, *41*(1).

Fukushima, Y., V. Cayol, and P. Durand (2005), Finding realistic dike models from interferometric synthetic aperture radar data: The February 2000 eruption at Piton de la Fournaise, *Journal of Geophysical Research-Solid Earth*, *110*(B3).

Massonnet, D., and K. L. Feigl (1998), Radar interferometry and its application to changes in the Earth's surface, *Reviews of Geophysics*, *36*(4), 441-500.

Masterlark, T., and Z. Lu (2004), Transient volcano deformation sources imaged with interferometric synthetic aperture radar: Application to Seguam Island, Alaska, *Journal of Geophysical Research-Solid Earth*, *109*(B1).

Mogi, K. (1958), Relations between the Eruptions of Various Volcanoes and the Deformations of the Ground Surfaces around them, *Bulletin of the Earthquake Research Institute*, *36*(2), 36.

Mossop, A., and P. Segall (1999), Volume strain within The Geysers geothermal field, *Journal of Geophysical Research: Solid Earth*, *104*(B12), 29113-29131.

Okada, Y. (1985), Surface Deformation Due to Shear and Tensile Faults in a Half-Space, *Bulletin of the Seismological Society of America*, *75*(4), 1135-1154.

Pollard, D. D., P. T. Delaney, W. A. Duffield, E. T. Endo, and A. T. Okamura (1983), Surface deformation in volcanic rift zones, *Tectonophysics*, *94*(1–4), 541-584.

Rizzo, F. J. (1967), An integral equation approach to boundary value problems of classical elastostatics, *Quart. Appl. Math.*, *25*, 13.

Sambridge, M. (1999), Geophysical inversion with a neighbourhood algorithm - I. Searching a parameter space, *Geophysical Journal International*, *138*(2), 479-494.

Segall, P. (2010), *Earthquake and Volcano Deformation*, 458 pp., Princeton University Press.

van Zwieten, G. J., R. F. Hanssen, and M. A. Gutiérrez (2013), Overview of a range of solution methods for elastic dislocation problems in geophysics, *Journal of Geophysical Research: Solid Earth*, *118*(4), 1721-1732.

Vanicek, P., R. O. Castle, and E. I. Balazs (1980), Geodetic leveling and its applications, *Reviews of Geophysics*, *18*(2), 505-524.

Vasco, D. W., C. Wicks, K. Karasaki, and O. Marques (2002), Geodetic imaging: reservoir monitoring using satellite interferometry, *Geophysical Journal International*, *149*(3), 555-571.

Wahba, G., and Y. H. Wang (1990), When is the optimal regularization parameter insensitive to the choice of the loss function, *Communications in Statistics-Theory and Methods*, *19*(5), 1685-1700.

Wright, T. J., B. E. Parsons, and Z. Lu (2004), Toward mapping surface deformation in three dimensions using InSAR, *Geophysical Research Letters*, *31*.